

FLORIDA STATE UNIVERSITY
COLLEGE OF ARTS & SCIENCES

THIS IS MY TITLE:
AND THIS IS ITS SECOND LINE

By
JULIA REAM

A Dissertation submitted to the
Department of Mathematics
in partial fulfillment of the
requirements for the degree of
Doctor of Philosophy

2023

Julia Ream defended this dissertation on July 11, 2023.

The members of the supervisory committee were:

Mark Sussman

Professor Co-Directing Dissertation

Marc Henry de Frahan

Professor Co-Directing Dissertation

Bryan Quaife

University Representative

Aseel Farhat

Committee Member

Sanghyun Lee

Committee Member

The Graduate School has verified and approved the above-named committee members, and certifies that the dissertation has been approved in accordance with university requirements.

Blah Blah Blah

ACKNOWLEDGMENTS

Blah Blah Blah

TABLE OF CONTENTS

List of Tables	viii
List of Figures	ix
List of Abbreviations	xi
Abstract	xii
1 Introduction	1
1.1 What is a Fluid?	1
1.1.1 Important Definitions	1
1.1.2 Density and Temperature and Pressure, Oh My!	1
1.1.3 Supercritical Fluids	1
1.2 Mathematics of Fluid Flow	2
1.2.1 Continuum Description of Fluids	4
1.2.2 Equation of State	6
1.3 Turbulence	7
1.3.1 Mathematics of Turbulence	8
1.3.2 Numerical Approaches to Turbulence Modeling	9
1.4 Supercritical Carbon Dioxide	12
1.4.1 Applications of Interest	13
1.4.2 Overview of Current Numerical Landscape	15
2 Model Overview	17
2.1 Introduction	17
2.2 Governing Equations	17
2.2.1 Transport Models	18
2.2.2 Thermodynamics and Related Quantities	19
2.2.3 Filtered Navier-Stokes Equations	21
2.2.4 Subgrid-Scale Modeling for Large Eddy Simulation	23
2.3 Validation	24
3 Algorithm Overview	25
3.1 Introduction	25

3.2	Numerical Methods	25
3.2.1	Piecewise Parabolic Method Overview	25
3.2.2	Approximate Riemann Solver Details	25
3.3	Error	25
4	Simulations	26
4.1	Computational Domain	26
4.1.1	AMReX and Discretization	26
4.1.2	Initial and Boundary Conditions	26
4.2	Case Descriptions	28
4.2.1	Parameter Choices	28
4.3	Compute Time and Hardware Specifications	28
4.4	Post-Processing Procedures	28
5	Results	29
5.1	Isothermal Jet	29
5.1.1	Flow Field Features	29
5.1.2	Mean Flow Properties	31
5.1.3	Turbulence Dynamics	34
5.2	Non-Isothermal Jets	36
5.2.1	Flow Field Features	36
5.2.2	Mean Flow Properties	36
5.2.3	Turbulence Dynamics	36
5.3	Discussion	36
6	Conclusion	37
6.1	Summary	37
6.2	Future Work	37
Appendix		
A	Transport Coefficients	38
A.1	EGLib Low Pressure Approximation Coefficients	38
A.2	Chung High Pressure Correction Coefficients	38

B Additional Thermodynamic Quantities	40
B.1 Ideal Gas NASA Polynomial Fit Coefficients	40
B.2 SRK Derivatives	40
Bibliography	42
Biographical Sketch	50

LIST OF TABLES

A.1	Linear Coefficients Used in Calculating High Pressure Viscosity Corrections as found by Chung et al. [10]	39
A.2	Linear Coefficients Used in Calculating High Pressure Thermal Conductivity Corrections as found by Chung et al. [10]	39
B.1	Linear Coefficients Used in Calculating High Pressure Viscosity Corrections as found by Chung et al. [10]	41
B.2	Linear Coefficients Used in Calculating High Pressure Thermal Conductivity Corrections as found by Chung et al. [10]	41

LIST OF FIGURES

1.1	Characteristic length scale of problem, L , compared to mean free path of particles, ℓ , for a flow with large Knudsen number (left) vs. small Knudsen number (right)	3
1.2	A fluid of arbitrary volume V bounded by surface S with velocity $\mathbf{v}(\mathbf{x}, t)$. A differential volume and surface area is given by dv and ds , respectively. \mathbf{n} is the outward-pointing unit normal vector to the surface S	4
1.3	Example of streamlines in laminar (left) vs. turbulent (right) flow.	7
1.4	Depiction of the energy cascade present in turbulence along associated scales. Resolved vs. Modeled scales are mapped for direct numerical simulation (DNS), large eddy simulation (LES), and Reynolds-averaged Navier-Stokes (RANS) [].	10
1.5	LES resolves large scale eddies (black) and models the effects of fine scale eddies (red) that are unresolved due to mesh size.	11
1.6	Phase diagram for Carbon Dioxide (CO ₂). Critical pressure, p_c , and temperature, T_c , are 73.773 bar and 304.128 K, respectively.	13
1.7	Size comparison for steam vs. supercritical Carbon Dioxide (sCO ₂) turbine via Echogen Power Systems LLC [44].	14
4.1	Two dimensional slice schematic of jet setup. Four levels of refinement are enforced within the green box based on proximity to jet inlet. Refinement based on vorticity criterion then occurs within the blue region. Outside the blue region, adaptive mesh refinement (AMR) is explicitly turned off to allow flow structures to be dissipated numerically and allowed to leave the domain without incurring spurious reflections.	27
5.1	Axial velocity features of the isothermal jet	30
5.2	Pressure features of the isothermal jet	30
5.3	Vorticity magnitude features of the isothermal jet	31
5.4	Average (both in time and radially) axial velocity scaled by inlet value plotted along radial distance from centerline. Profile decay follows similar trajectory to what is expected in incompressible round jet theory [46].	32
5.5	Normal slices of scaled axial velocity, averaged in both time and the radial direction. Plotted against radial direction scaled by $r_{1/2}$. Both near- and far-field regions demonstrate the self-similarity within the round turbulent jet.	33
5.6	Axial inlet velocity scaled by centerline values along the axial direction. When distance downstream is scaled by jet diameter, linear decay of the centerline axial velocity is observed.	34

5.7	Time and radially averaged Reynolds stresses for the isothermal jet at two locations downstream. Both slices follow similar Reynolds stress relations as seen in incompressible round jet [46].	35
5.8	Average turbulent kinetic energy components along centerline.	35

LIST OF ABBREVIATIONS

The following short list of abbreviations are used throughout this document.

AMR	Adaptive Mesh Refinement
CFD	Computational Fluid Dynamics
CO ₂	Carbon Dioxide
DNS	Direct Numerical Simulation
DOE	Department of Energy
ECP	Exascale Computing Project
EoS	equation of state
HPC	high-performance computing
LES	Large Eddy Simulation
NIST	National Institute of Standards and Technology
NREL	National Renewable Energy Laboratory
PPM	piecewise parabolic method
PR EoS	Peng-Robinson equation of state
RANS	Reynolds-Averaged Navier-Stokes
rms	root mean square
sCO ₂	Supercritical Carbon Dioxide
SGS	Subgrid Scale
SMD	dynamic Smagorinsky
SRK EoS	Soave-Redlich-Kwong equation of state

ABSTRACT

Blah Blah Blah

CHAPTER 1

INTRODUCTION

Fluids are a vital part of everyday life - two of the most common ones being the air we breath and the water we drink. Less obvious are all the ways even these common fluids function behind the scenes in our day to day activities. Water, for example, serves an important role in various industrial settings, proving useful in areas ranging from thermal management to energy production; steam turbines alone accounted for 45% of electricity generation in the United States in 2021 [59]. Improvements to these types of systems impact technologies across a variety of fields and are thus an important area of research. One strategy toward this end, and the primary motivator of the work presented here, is the use of supercritical fluids as the working fluid of these systems.

1.1 What is a Fluid?

In order to discuss supercritical fluids further, we must first go into more detail about general fluids. A *fluid* is a large collection of mutually interacting particles (e.g., molecules, atoms, etc.) in a state of constant and chaotic motion. This results in the continuous deformation of the substance under the effects of a shearing stress. The two categories of fluids that most people are familiar with are gases and liquids. *Liquids* are (mostly) incompressible and have definite volume for a set temperature and pressure. *Gases* are compressible and do not have definite volume. A simplified distinction between the two is that both gases and liquids will conform to the shape of whatever container they are in, but gases will further spread to fill all available space present.

1.1.1 Important Definitions

1.1.2 Density and Temperature and Pressure, Oh My!

1.1.3 Supercritical Fluids

A *supercritical fluid* is a fluid that is held above a critical temperature and pressure, at which point the distinction between a gas and liquid phase no longer exists [19, 60]. Supercritical fluids have qualities associated with both gases and liquids yet simultaneously have features that exclude them from fully being categorized as one or the other. For example, while they have viscosities akin to gases, they have solvent capabilities associated with liquids []. Similarly, while they have densities

in line with liquids, they lack surface tension [1]. One benefit of this duality is that supercritical fluids can be fine tuned to be more gas-like or more liquid-like depending on the application at hand. This also results in ambiguity on how to actually classify them, with some sources considering them highly compressed gases [23], expanded liquids [1], or even as their own distinctly separate phase [6]. The distinction usually lies on the specifics of the regime and the application at hand.

This work is concerned with supercritical Carbon Dioxide (sCO₂) in particular. sCO₂ has many beneficial features to a wide variety of industrial applications, as we will detail further in section [1]. Many of the applications of interest to this work involve injection technologies that require a round turbulent jet configuration within the system. While much research has gone into sCO₂ flows, the current landscape is lacking in turbulence of this type with the context of understanding the underlying physics relating to the flow itself. For research that does involve other supercritical turbulent jets, the regimes explored in those works typically involve transcritical fluid injection within the regime of interest or explore regions outside the scope of this work.

The goal of this work is to explore the pseudo-boiling region of the pseudo-critical zone and analyze the influence of extreme thermodynamic fluctuations on turbulence statistics within the flow field. To that end, the rest of this chapter continues as follows: first, the mathematical framework for modeling compressible Newtonian fluids is provided to form the basis of the modeling done in this dissertation. Further consideration is then given to turbulence modeling and the numerical methods developed for studying turbulence to provide insight into the quantities of interest analyzed within this dissertation and the choices of numerical methods used herein. Important applications of supercritical carbon dioxide in particular are provided to motivate the problem presented in this dissertation. Existing numerical studies on supercritical fluids are reviewed to demonstrate how this dissertation fits into the current landscape of research and to emphasize the contribution the results of this work make to the field. This chapter concludes with an outline of the dissertation, the goals of the dissertation, and the main contributions made through this work.

1.2 Mathematics of Fluid Flow

Scale is one of the key factors to consider when developing a mathematical description of a fluid system. For example, consider modeling flow past a satellite in the exosphere vs. the flow past a turtle in the ocean; these two mediums have vastly different characteristics and would thus require different modeling techniques. Scale is also an important concept when it comes to turbulence in

particular so we will begin that discussion here with our choice in perspective for the mathematical framework of our system of interest.

From a kinetics perspective, particle motion within a fluid can be broken up into two phases: particle interaction and free flight. Average time spent in free flight, $\langle t_f \rangle$, is typically much greater than collision time for a given interaction, t_c . The average length traveled between collisions is known as the mean free path, ℓ . Since free flight time dominates particle interaction time, this phase determines the length scale of the kinetic description of motion. In addition to this inherent physical scale, there is also a scale associated with the resolution of the problem itself, L . These two scales are important, as the mathematical description of your model depends on how these two scales compare to one another. This comparison is related through the non-dimensional Knudsen number:

$$Kn = \frac{\ell}{L} \quad (1.1)$$

Flows with large Knudsen number ($Kn \gg 10$) require modeling from the kinetic or microscopic perspective as particle interactions become sparse enough compared to the scope of the problem to require a statistical mechanics framework. On the other hand, small Knudsen number flows ($Kn \ll 0.01$) have a problem scale that far exceeds the particle-level interactions present, giving way to an average overall motion within the fluid. This scale dichotomy is demonstrated with the graphic in Figure 1.1. For small Knudsen flows, a continuum description of the fluid is appropriate for capturing this macroscopic behavior.

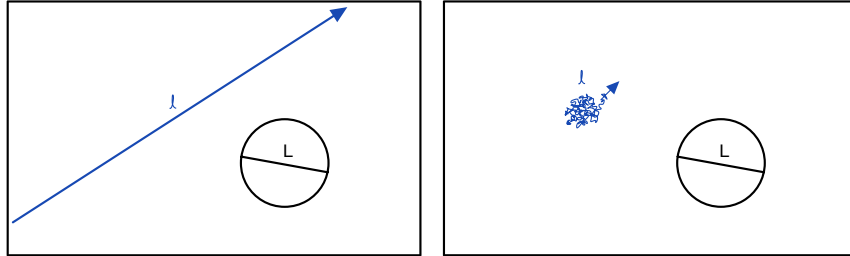


Figure 1.1: Characteristic length scale of problem, L , compared to mean free path of particles, ℓ , for a flow with large Knudsen number (left) vs. small Knudsen number (right)

This work falls within the small Knudsen regime, so we will be working with the continuum description of fluids. In this section we will discuss the Navier-Stokes Equations that arise from this modeling technique and how we account for the supercritical nature of the flow through our choice of equation of state.

1.2.1 Continuum Description of Fluids

The continuum hypothesis assumes that the fluid has no fine structures and that it is perfectly continuous, i.e., the properties of a small subdivision are the same as other subdivisions. This allows for the approximation of physical quantities at the infinitesimal limit [27].

For example, consider a fluid with arbitrary volume V as depicted in Figure 1.2.

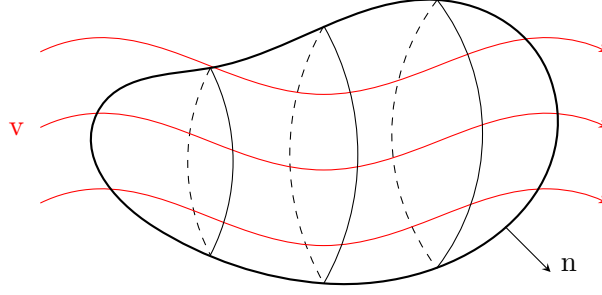


Figure 1.2: A fluid of arbitrary volume V bounded by surface S with velocity $\mathbf{v}(\mathbf{x}, t)$. A differential volume and surface area is given by dv and ds , respectively. \mathbf{n} is the outward-pointing unit normal vector to the surface S .

For a fluid with density $\rho(\mathbf{x}, t)$, mass within a small representative volume can be described with

$$\rho dv$$

Total mass in the arbitrary volume is then given by

$$\iiint_V \rho dv$$

The rate of change of mass through the volume is now

$$\begin{aligned} & \frac{d}{dt} \iiint_V \rho dv \\ &= \iiint_V \frac{\partial \rho}{\partial t} dv \end{aligned} \tag{1.2}$$

Simultaneously, overall change in mass throughout the volume can be described by the net mass flux through the surface S . Volumetric flow through a small portion of the bounding surface is given by

$$\mathbf{v} \cdot \mathbf{n} ds$$

Total mass flux through the entire surface is then

$$\iint_S \rho \mathbf{v} \cdot \mathbf{n} \, ds \quad (1.3)$$

Applying the divergence theorem to Eq. 1.3 yields the following volume integral

$$\iiint_V \nabla \cdot (\rho \mathbf{v}) \, dv \quad (1.4)$$

Assuming there is no additional source generating or leaking mass within the control volume, we can relate Eqs. 1.2 to 1.4 :

$$\begin{aligned} \iiint_V \frac{\partial \rho}{\partial t} \, dv &= - \iiint_V \nabla \cdot (\rho \mathbf{v}) \, dv \\ \iiint_V \frac{\partial \rho}{\partial t} \, dv + \iiint_V \nabla \cdot (\rho \mathbf{v}) \, dv &= 0 \\ \iiint_V \left(\frac{\partial \rho}{\partial t} + \nabla \cdot (\rho \mathbf{v}) \right) \, dv &= 0 \end{aligned} \quad (1.5)$$

Note the inclusion of the negative sign for the right side of the initial equality; in the surface integral formulation, the outward facing normal describes flux out of the volume, thus yielding a decrease in mass within the volume. Since Eq. 1.5 holds for any arbitrary volume V , the integrand must be identically equal to zero:

$$\frac{\partial \rho}{\partial t} + \nabla \cdot (\rho \mathbf{v}) = 0 \quad (1.6)$$

Through the continuum hypothesis and conservation of mass, we have now arrived at the continuity equation in Eq. 1.6. This specific process demonstrates an even more fundamental relationship known as a *conservation law*. More generally, for some integrated property ϕ , the rate of change of ϕ within a control volume must be equal to the amount of ϕ lost or gained through the boundaries of the control volume plus what is created or consumed by any sinks or sources, s , within the volume (sinks having positive orientation to match the positive orientation of the outward-facing normal \mathbf{n}) [].

$$\frac{\partial \phi}{\partial t} + \nabla \cdot (\phi \mathbf{v}) + s = 0 \quad (1.7)$$

In addition to this concept applying to conservation of mass, as was seen in this section, the idea outlined by Eq. 1.7 applies to conservation of momentum and energy within the fluid. Together, these expressions combine to form the basis of the Navier-Stokes Equations, as will be seen in more detail in chapter 2. The important takeaway from this section is that with the continuum hypothesis and fundamental laws of physics, one can adequately capture macroscopic flow behavior for the types of flows we are interested in within this work.

1.2.2 Equation of State

Conservation of mass, momentum, and energy gives us five equations to describe our fluid system. For compressible flows, this is not enough information to solve for all the unknowns within the system of coupled partial differential equations. A sixth equation, known as the Equation of State (EoS), must be chosen in order to close the system. The EoS relates three of the six unknowns: pressure, temperature, and density. Here we will briefly discuss some EoS options and their distinguishing characteristics in order to motivate the choice made for this work.

The simplest option available is the ideal gas EoS, which comes from the ideal gas law. This EoS relates density, pressure, and temperature in the following manner:

$$p = \frac{RT}{V_m} \quad (1.8)$$

where p is pressure, R is the universal gas constant, T is temperature, and $V_m = \frac{V}{n}$ is the molar volume of the fluid (it is common to express density in terms of molar volume for sake of simplicity in writing the EoS with V being volume and n being the number of moles). The ideal gas EoS is fairly accurate for liquids and gases at moderate temperatures and low pressures. It fails at low temperatures and high pressures, especially near the transition region from gas to liquid. The inaccuracy noted in this region means this EoS would not be suitable for the area of interest within this study.

Cubic EoS generally provide more accuracy than the ideal gas EoS. The first cubic EoS was developed by van der Waal in 1873, modifying the ideal gas EoS to take into consideration the finite size of molecules and interactions between molecules (the ideal gas EoS only accounts for interactions with the container and treats molecules as point particles). Other cubic EoS can be thought of as modifications from this base form:

$$p = \frac{RT}{V_m - b} - \frac{a}{V_m^2} \quad (1.9)$$

where a and b are constants related to the pressure and temperature at the critical point, p_c and T_c respectively:

$$a = \frac{27(RT_c)^2}{64p_c}, \quad b = \frac{RT_c}{8p_c}$$

One of the main benefits of using a cubic EoS is that they can have comparable and sometimes even better accuracy compared to their higher order counterparts, thus reducing computational costs. However, it is important to take into consideration the regime of interest in addition to

the fluid of interest when choosing an EoS, as each one has its own pros and cons. For example, molecule polarity and density are two factors that can have a high impact in selection between the Soave-Redlich-Kwong Equation of State (SRK EoS) and Peng-Robinson Equation of State (PR EoS) alone [22].

This work uses the SRK EoS as will be more thoroughly introduced in chapter 2. It has been shown that this equation of state is fairly accurate for the parameter regime under careful consideration in this work []. This accuracy is detailed further in chapter 3 through comparisons with data from National Institute of Standards and Technology (NIST). Overall, when adequately considered, the EoS is the key avenue to incorporating specific fluid properties into the mathematical model.

1.3 Turbulence

In addition to categorizing by fluid type, fluid flow can be categorized based on flow characteristics. The main two classifications of note are laminar flow and turbulent flow.

Laminar flow is denoted by fluid particles having well-defined parallel trajectories of motion, or streamlines. Streamlines do not cross, meaning adjacent layers within the fluid flow by one another with little to no mixing. From a more generalized perspective, the flow appears to be smooth. In contrast to this, turbulent flow is characterized by its unpredictable and chaotic trajectories. Streamlines do cross resulting in swirls and eddies of varying length scales which induce mixing. Turbulent flow can be qualitatively described as being rough due to this high degree of fluctuation within the velocity and pressure fields present. This generalized description is depicted in Figure 1.3.

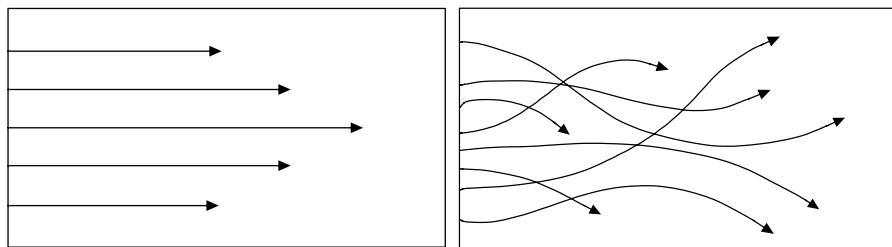


Figure 1.3: Example of streamlines in laminar (left) vs. turbulent (right) flow.

The Reynolds number is a dimensionless value that can be used to distinguish laminar flow from turbulent flow. It is defined as follows:

$$\text{Re} = \frac{\rho u L}{\mu} \quad (1.10)$$

where ρ and μ are the density and dynamic viscosity of the fluid, respectively, u is the flow velocity, and L is a characteristic length scale associated with the given flow scenario (e.g., pipe diameter). As is demonstrated by the ratio in Equation 1.10, the Reynolds number measures the relative effects of inertial forces compared to viscous forces within a given flow scenario. A small Reynolds number signifies the dominance of viscous forces; fluid parcels moving in tandem want to “stick together,” resulting in the sheared flow and parallel trajectories seen in laminar flow. Turbulence is then characterized by a large Reynolds number, where inertial forces take precedence. Here, deviations within the laminar flow field result in lateral mixing between shear layers. This creates eddies and random trajectories that result in the chaotic motion of turbulent flow.

This work focuses on the turbulent round jet and its associated dynamics in the context of supercritical fluids. The remainder of this section details a brief overview of important turbulence concepts and numerical methods developed for studying turbulence in order to motivate the modeling and numerical choices made within this work.

1.3.1 Mathematics of Turbulence

Turbulence has been recognized and investigated by scholars in some way, shape, or form for thousands of years; Lucretius being one of the earliest, describing eddy motion in his *De rerum natura* [7]. In that time, a comprehensive theory of turbulence has still not been reached. There are, however, many widely accepted hypotheses and models that at least in part explain certain aspects of turbulent flows.

Turbulent motion contains a wide range of scales. Richardson formalized this concept by describing turbulence as a compositions of eddies, each with their own characteristic size and velocity [1]. From this perspective, large eddies are said to be unstable and break up into smaller eddies, transferring energy down the line to smaller and smaller eddies. This energy cascade continues down to the molecular level where it is dissipated through molecular viscosity. Kolmogorov further developed this theory, noting that for sufficiently high Reynolds flow, the statistics of these smallest-scale motions are uniquely determined by the kinematic viscosity of the fluid, ν , and the dissipation rate, ε [2]. These smallest eddy length, velocity, and time scales at which dissipation

occurs, known as the Kolmogorov scales, are defined as follows:

$$\begin{aligned}\eta &\equiv (\nu^3/\varepsilon)^{1/4}, \\ u_\eta &\equiv (\nu\varepsilon)^{1/4}, \\ \tau_\eta &\equiv (\nu/\varepsilon)^{1/2}\end{aligned}\tag{1.11}$$

While the continuum description introduced in the previous section is still valid for turbulent flows, this vast scale separation and the random nature of fluctuations across these scales, including a dependence on problem-specific flow configurations and boundary conditions, make universal solutions to these types of problems unattainable. To that end, numerical simulations are invaluable in studying turbulence phenomena.

1.3.2 Numerical Approaches to Turbulence Modeling

A vast array of numerical approaches have been developed to tackle the modeling challenges inherent to turbulence, with further development of these and new techniques remaining an active field of research today. We will briefly look at three families of numerical simulation methods in order to highlight the challenges associated with the large scale disparity included in turbulent flows. Methods of note include use of the Reynolds-Averaged Navier-Stokes (RANS) equations, direct numerical simulation (DNS), and large eddy simulation (LES), with scale coverage of each outlined in Figure 1.4.

At one extreme, we have DNS. The aim of DNS is to resolve all scales within the turbulent flow, from the largest eddies down to the Kolmogorov scale. To do this, all components of the Navier-Stokes equations are discretized and numerically advanced. Numerical methods may include high-order finite differencing or pseudo-spectral methods depending on the type of turbulence, flow configuration, and boundary conditions at hand. While DNS can capture physics across all scales of the flow with high accuracy, this comes at a steep computational cost. Grid spacing and time stepping are highly dependent upon the Reynolds number (approximately as Re^3 [46]). Thus DNS very quickly becomes limited to lower Reynolds flows, even with high computing resources.

On the other end of the spectrum, we have RANS modeling. The RANS equations make use of the Reynolds decomposition of the flow, in which a random velocity field \mathbf{u} can be split into an ensemble average, $\langle \mathbf{u} \rangle$, and a fluctuating component, \mathbf{u}' , such that:

$$\begin{aligned}\mathbf{u}'(\mathbf{x}, t) &\equiv \mathbf{u}(\mathbf{x}, t) - \langle \mathbf{u}(\mathbf{x}, t) \rangle, \\ \langle \mathbf{u}(\mathbf{x}, t) \rangle &= \lim_{N \rightarrow \infty} \frac{1}{N} \sum_{i=1}^N \mathbf{u}_i(\mathbf{x}, t)\end{aligned}\tag{1.12}$$

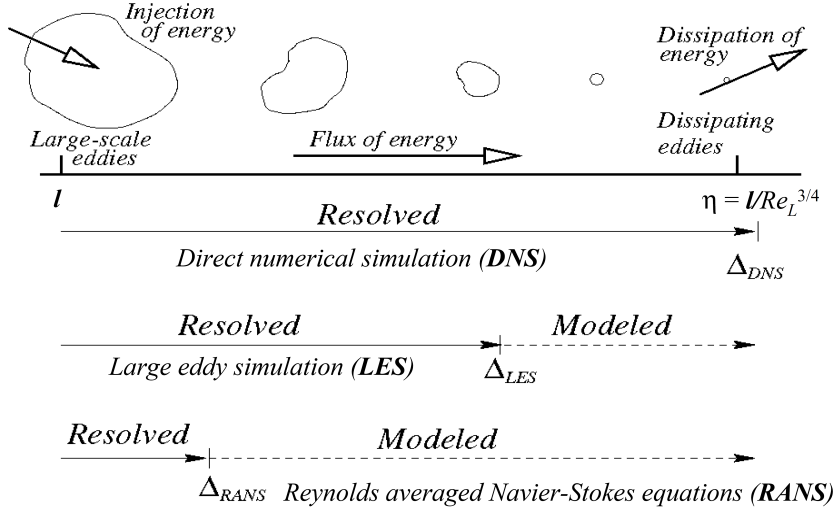


Figure 1.4: Depiction of the energy cascade present in turbulence along associated scales. Resolved vs. Modeled scales are mapped for DNS, LES, and RANS [].

where i is the i – th realization of a flow of identical conditions with the number of realizations N tending toward infinity. In practice, for numerical models with the RANS equations, this is implemented via time averaging:

$$\langle \mathbf{u}(\mathbf{x}, t) \rangle \approx \overline{\mathbf{u}(\mathbf{x})} \equiv \frac{1}{T} \int_{t_0}^{t_0+T} \mathbf{u}(\mathbf{x}, s) ds$$

where T is taken to be much larger than the time scale of the fluctuating components. By substituting $\mathbf{u}(\mathbf{x}, t) = \overline{\mathbf{u}(\mathbf{x})} + \mathbf{u}'(\mathbf{x}, t)$ particular substitution into the Navier-Stokes equations, one can get a statistical description of the average flow field for the turbulent system (note - the more general decomposition given in equation 1.12 can be used in the substitution as well to take into consideration a moving average within the flow field. For many of the applications in which RANS is used, it is enough to look at the steady state given by the time averaged system). Further equations are then needed to model the additional stresses that arise from the nonlinear interactions between components of the mean flow field. Overall, simulations of the RANS equations resolve the larger scale motions associated with the average motion of the field in a statistical description of the system while the influence of fluctuating fields are incorporated via modeling. While this reduces the computational cost of the numerics, more closure issues arise from the modeling requirements

introduced, which present a whole new set of choices and assumptions that are highly problem specific.

Finally, we have LES, which falls between the two extremes of the methodology spectrum presented thus far. The strategy with LES is to only resolve the energy containing scales in the system and model the influence of the smaller scales, as demonstrated in Figure 1.5. This allows for some relaxation in computational cost compared to DNS without introducing the same degree of modeling assumptions required for RANS. While still fairly computationally expensive overall, LES can resolve more of the instantaneous flow field and capture certain physics that inherently depend on the small scale dynamics; quantities of this nature are lost or become highly model dependent in RANS which introduces more error to the simulation.

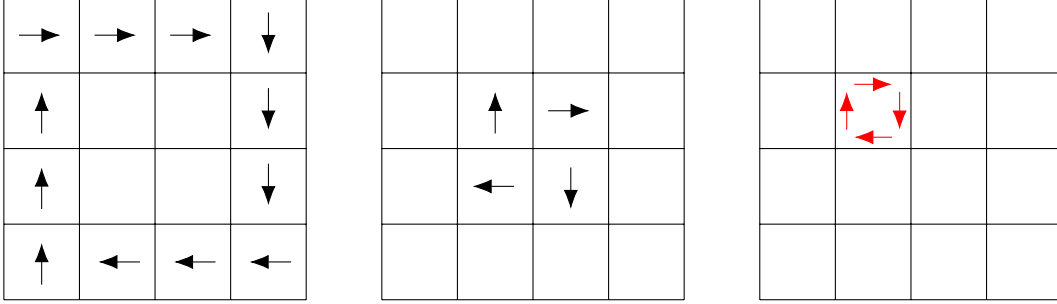


Figure 1.5: LES resolves large scale eddies (black) and models the effects of fine scale eddies (red) that are unresolved due to mesh size.

The procedure for LES involves decomposing random velocity field \mathbf{u} into filtered components, $\bar{\mathbf{u}}$, and residual components, \mathbf{u}'' , such that:

$$\begin{aligned}\mathbf{u}''(\mathbf{x}, t) &\equiv \mathbf{u}(\mathbf{x}, t) - \bar{\mathbf{u}}(\mathbf{x}, t), \\ \bar{\mathbf{u}}(\mathbf{x}, t) &= \int_{-\infty}^{\infty} \int_{-\infty}^{\infty} \mathbf{u}(\mathbf{r}, s) G(\mathbf{x} - \mathbf{r}, t - s) d\mathbf{r} ds\end{aligned}\tag{1.13}$$

G is the convolution kernel of associated filter spatial and/or temporal cutoff Δ and τ_c , respectively, satisfying $\int_{-\infty}^{\infty} \int_{-\infty}^{\infty} G(\mathbf{r}, s) d\mathbf{r} ds = 1$. In practice, common kernels are only spatially dependent. Applying this filtering procedure to the Navier-Stokes equations yields an additional term known as the residual stress tensor that must be modeled. The filtered Navier-Stokes equations can then be discretized to numerically simulate the large eddy behavior of the system.

This general LES procedure may seem similar to what was described for the RANS model, especially in terms of the decomposition of the flow field, but there are key differences to note.

Conceptually, the result of a numerical simulation using RANS describes an average behavior of turbulent flow over many instances or experiments. The output of these simulations is not a snapshot of one instance of the given flow field but rather an approximation to how the flow behaves in a statistical sense. LES does approximate a single realization of the flow field, just only including the low frequency modes of the system which contain the majority of the energy. Additionally, the components of the Reynolds decomposition obey the following rules:

$$\overline{\overline{\mathbf{u}}} = \overline{\mathbf{u}}, \quad \overline{\mathbf{u}'} = 0$$

These rules do not hold for $\overline{\mathbf{u}}$ and \mathbf{u}'' :

$$\overline{\overline{\mathbf{u}}} \neq \overline{\mathbf{u}}, \quad \overline{\mathbf{u}''} \neq 0$$

We use LES in this work to balance the computational cost of the simulation with the degree of resolution for physical phenomena within the flow. Many studies involving turbulent supercritical fluids utilize LES, as will be seen in the next section, with additional research having been conducted regarding appropriate choices in modeling for the residual stress tensor. Model selection and further details on filtering are discussed in Chapter 2.

1.4 Supercritical Carbon Dioxide

As mentioned earlier, supercritical fluids have many qualities that make them desirable as working fluids in a variety of systems. We now shift our focus to one particular fluid of interest: Carbon Dioxide (CO₂). As seen in the phase diagram of Figure 1.6, the critical temperature, T_c , and critical pressure, p_c , of CO₂ are 304.128 K and 73.773 bar. The critical temperature and pressure of CO₂ is fairly easy to attain, making it a strong candidate for systems with high thermal outputs. Additionally, sCO₂ has a relatively low toxicity and environmental impact [1], and is chemically stable, non-flammable, and readily available [2]. For these reasons, sCO₂ is a highly coveted alternative working fluid in many different applications, and is one of the most widely used supercritical fluids along with water [19].

In the next part of this section, we will explore some applications of sCO₂ in which the turbulent round jet configuration is used. Then we will go through a brief review of recent studies involving sCO₂, and more generally supercritical turbulent jets, in order to demonstrate where this work fits in among current research. Finally, we outline the structure of the remainder of the dissertation.

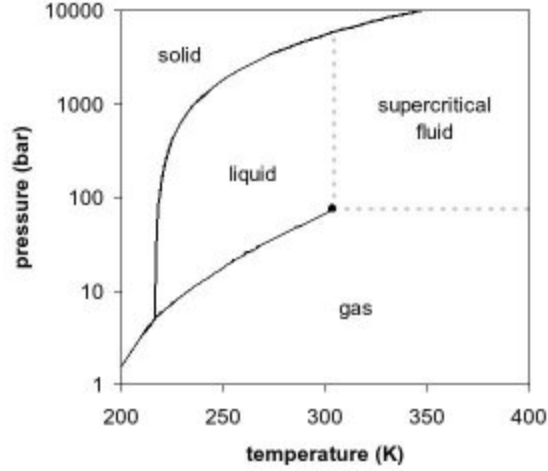


Figure 1.6: Phase diagram for Carbon Dioxide (CO₂). Critical pressure, p_c , and temperature, T_c , are 73.773 bar and 304.128 K, respectively.

1.4.1 Applications of Interest

One of the key applications of interest that motivates this work is the use of sCO₂ as the working fluid in advanced cycles for power generation. sCO₂ has shown promise as a working fluid for both indirect cycle and direct-firing cycles [65, 66]. One example of indirect cycle improvement uses sCO₂ in place of water for the conventional steam-Rankine cycle. An example of where these types of configurations may prove useful is in managing thermal runoff from existing coal and natural gas combustion processes [65]. Compared to steam, sCO₂ is less corrosive, more thermally stable, and has increased power density. The critical point of CO₂ is easily accessible, and once achieved, allows for the use of a single phase fluid design, leading to a simplified and more compact turbine (see Figure 1.7). Ultimately, this also allows for lower operation and maintenance costs [14]. The benefits of using sCO₂ turbines over the traditional steam design has been highly researched and has only seen an increase in momentum for implementation [13, 16, 14, 44].

An example of direct-firing cycles that use sCO₂ include the Allam cycle [4]. When compared to the conventional Brayton cycle, studies show that the Allam cycle has much higher efficiency [15, 5]. Additionally, the carbon footprint for the Allam cycle is virtually zero, allowing for CO₂ produced from the system to be stored underground or used elsewhere, aiding in carbon sequestration efforts [20]. This two-for-one benefit of using sCO₂-based cycles such as the Allam cycle has spurred much research [63, 9] and development [51] into related technologies.

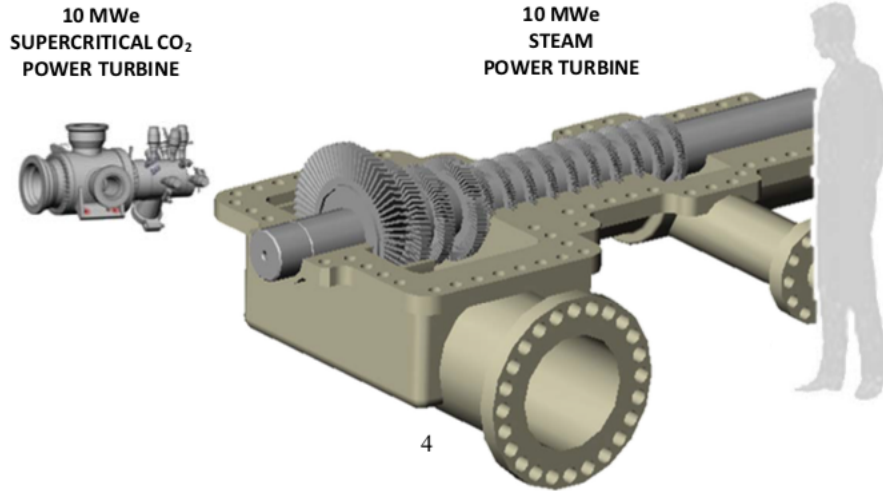


Figure 1.7: Size comparison for steam vs. sCO₂ turbine via Echogen Power Systems LLC [44].

Of particular importance to these applications is the round turbulent jet, as this is a major component of many injection technologies. The high densities associated with the liquid-like aspect of supercritical fluids coupled with the relatively low gas-like viscosity associated with them typically results in a high Reynolds flow, often resulting in a turbulent system. The turbulence physics of these jets is crucial in developing machinery for these systems. Current experimental research is mainly application oriented. Research into the sCO₂ jet's rock breaking ability has been of primary importance to Enhanced Geothermal Systems (EGS) applications [47, 48, 34, 56, 32], with additional focus being given to pipeline leakage and flow dynamics upon wall impact [62, 61], which unfortunately does not explore the underlying turbulence statistics of the flow. Enhanced recovery of unconventional reservoirs for oil and gas development is an additional area where rock breaking research is often applied [26, 25]. Chemical engineering design aspects of sCO₂ injection are more focused on solubility dynamics as opposed to turbulence [28, 30]. Other experiments focus on similar application specific quantities of interest, such as heat transfer and mixing, which is related in part to the turbulence dynamics [68, 35], but they also note the difficulty in experimental design for investigating these aspects of the flow under the conditions needed to replicate those in real applications [28]. Thus, numerical simulations are necessary to further explore the turbulence statistics of these flows.

1.4.2 Overview of Current Numerical Landscape

Numerical simulations are a necessary tool for investigating many aspects of supercritical flow fields due to the often challenging nature of experiment design for the extreme conditions inherent to these systems. Studies using DNS have been implemented to help establish benchmark test cases for other types of numerical schemes [43, 55]. Ruiz et al. use 2D DNS to simulate a mixing layer created by two streams of supercritical Oxygen and gaseous Nitrogen, using two different computational fluid dynamics (CFD) solvers to add confidence to their results [52]. A 3D DNS is used by Ries et al. to simulate a round Nitrogen jet for comparison with experimental data produced by Mayer et al. [50]. However, this study requires a reduction in Reynolds number from 1.62×10^5 , based on the injection diameter, to 5300 in order to feasibly execute the computations. Li also utilizes a low Reynolds number of 1750 to study a round turbulent sCO₂ jet with a preconditioning scheme [31]. The RANS approach has also been implemented utilizing theory from the ideal gas case [37], but with the goal of ascertaining a more general understanding of why specifically sCO₂'s rock-breaking ability is better than that of water.

Much research has gone into the development of appropriate numerical methods for investigations regarding turbulence in supercritical fluids. In order to maintain a high Reynolds flow and better capture the effects of the supercritical nature of the fluid on the turbulence dynamics, the use of LES has been explored. The impact of subgrid-scale (SGS) models in capturing transcritical and supercritical dynamics of cryogenic Nitrogen have been analyzed through comparison with the Mayer et al. experiment and highly accurate NIST data [45, 71, 72, 42, 64]. Schmitt et al. does a similar investigation using LES, then extending their investigation to include sCO₂ after validation with the Mayer et al. data [54]. However, this investigation uses low-pressure jets and does note the SGS models might need additional contributions to handle non-linearities and the pressure regime. While many of these investigations note that SGS models may need modification to deal with supercritical flows [54, 45, 42, 71], it is noted by Muller et al. that given a sufficiently fine grid, the influence of SGS modeling and numerical flux discretization is essentially limited to second-order moments [42]. Thus, we will be using the compressible version of the dynamic Smagorinsky SGS closures for our investigation, with further consideration of any influence of SGS model on our quantities of interest being noted later on.

Many of the numerical investigations cited thus far consider cryogenic nitrogen in order to compare with the Mayer et al. experiment on supercritical jet turbulence [39]. A wide variety

of numerical investigations into jet turbulence using sCO₂ exist but typically explore either other parameter regimes of interest or application-specific quantities of interest. Examples of turbulent adjacent quantities of interest include fluctuation characteristics based on inlet conditions [70], effects of nozzle and aperture differences on pressure and velocity decay [8] and wave features [36], mixing between sCO₂ and other fluid phases [49], and energy dissipation [33]. These studies all involve high pressure jets and are commonly found in applications involving rock fracturing. Related configurations are also studied, such as the swirling-round sCO₂ jet [67], turbulent jet-in-crossflows [69], slot jet impingement [3], and channel flow [2].

While much of the literature thus far has explored the impact of different numerical methods on modeling supercritical fluid flows and has aimed to strengthen the validity of these simulations in spite of the lack of experimental data available in the current landscape, a general consensus has still not been reached on how the supercritical nature of these fluids impacts the turbulence physics of these models. Thus, there remain open questions for understanding the fundamental flow behavior of turbulent jets in a supercritical environment, especially near the supercritical point, where both experimental and numerical investigations are still a challenge.

Our objective is to use LES to investigate the turbulence physics of sCO₂ near the critical point in order to capture the effects of widely varying thermal properties of supercritical fluids. Using the compressible Navier-Stokes equation solver, *PeleC* [osti/1374142], closed with the SRK EoS, we consider three cases in order to examine various quantities of interest associated with classical turbulence mechanics. These three cases are chosen to capture different areas around a peak in specific heat that is associated with the pseudo-critical region. The rest of this dissertation is outlined as follows. Chapter 2 details the model used for this study and gives an overview of the numerical methods implemented through *PeleC*. Chapter 3 outlines the simulation setup with parameter choices and validation. Results for cross-case comparisons and comparisons with external work are then presented in Chapter 4, with a summary and future work detailed in Chapter 5.

CHAPTER 2

MODEL OVERVIEW

2.1 Introduction

This section details the governing equations and numerical methods used to simulate the sCO₂ jet. As introduced previously, the compressible Navier-Stokes equations form the basis of the model along with the SRK EoS. Here we also detail the filtering used in the LES and the dynamic Smagorinsky (SMD) used to model the SGS dynamics [38].

To discretize and evolve the system of partial differential equations, including the LES SGS terms, we use *PeleC*, a compressible hydrodynamics code for reacting flows that leverages *AMReX* for AMR [24, 57]. *PeleC* is a highly scalable code for heterogeneous architectures that is being developed as part of the Exascale Computing Project (ECP) through the Department of Energy (DOE). It leverages the *PelePhysics* library for complex physics, including chemical reactions, non-ideal EoS, and high fidelity transport models. For spatial discretization, *PeleC* contains a few variations of the general piecewise parabolic method (PPM) originally derived by Colella and Woodward [11]. We utilize a variation that allows for extrema preservation in the presence of steep gradients [41, 12]. For time discretization, a second order Runge-Kutta scheme is used, and the time step is dynamically limited using a Courant number of 0.9.

2.2 Governing Equations

We consider the three-dimensional compressible Navier-Stokes equations, presented here with Einstein notation:

$$\frac{\partial \rho}{\partial t} + \frac{\partial}{\partial x_j} (\rho u_j) = 0, \quad (2.1a)$$

$$\frac{\partial}{\partial t} (\rho u_i) + \frac{\partial}{\partial x_j} (\rho u_i u_j + p \delta_{ij} - \sigma_{ij}) = 0, \quad (2.1b)$$

$$\frac{\partial}{\partial t} (\rho E) + \frac{\partial}{\partial x_j} ((\rho E + p) u_j + q_j - \sigma_{ij} u_i) = 0 \quad (2.1c)$$

where ρ is the density, u_j is the velocity for the x_j direction, p is the pressure, $E = e + \frac{u_i u_i}{2}$ is the total energy, e is the internal energy, and T is the temperature. Following the assumptions made

for Newtonian fluids [], the diffusive fluxes are

$$\sigma_{ij} = 2\mu S_{ij} - \frac{2}{3}\mu\delta_{ij}S_{kk}, \quad q_j = -\lambda\frac{\partial T}{\partial x_j} \quad (2.2)$$

where $S_{ij} = \frac{1}{2}\left(\frac{\partial u_i}{\partial x_j} + \frac{\partial u_j}{\partial x_i}\right)$ is the strain-rate tensor, μ is the dynamic viscosity, and λ is the thermal conductivity. Models regarding these two components are given in more detail in the next section. δ_{ij} here is the Kronecker delta. External forces such as gravity are not included in this study. The system is closed using the SRK EoS [58] to relate pressure, density, and temperature as follows:

$$\begin{aligned} p &= \frac{RT}{V_m - b} - \frac{a\alpha}{V_m(V_m + b)}, \\ a &= \frac{0.42747R^2T_c^2}{P_c}, \\ b &= \frac{0.08664RT_c}{P_c}, \\ \alpha &= \left(1 + (0.48508 + 1.55171\omega - 0.15613\omega^2)(1 - T_r^{0.5})\right)^2 \end{aligned} \quad (2.3)$$

where R is the ideal gas constant, T_c and P_c are the critical temperature and pressure of the species, respectively, $T_r = T/T_c$ is the reduced temperature given by the ratio of the absolute temperature to the critical temperature, V_m is the molar volume of the species, and ω is the acentric factor of the species. All cases are run with a single species, that being CO₂.

2.2.1 Transport Models

Modeling of transport coefficients is done through *PelePhysics* []. There are three modeling options available in *PelePhysics*; we use the *Simple* model. The *Simple* model approximates ideal gas transport coefficients using EGLib functions [18], which have the following form:

$$\ln(q_0) = \sum_{n=1}^4 a_{q,n} (\ln(T))^{n-1} \quad (2.4)$$

where q_0 is the transport quantity of interest (either λ or μ) and a is the appropriate pre-calculated polynomial fit coefficient (see Appendix ??). Chung's high pressure correction for viscosity and thermal conductivity are included to account for real gas dynamics [10]:

$$q = q_k + q_p \quad (2.5)$$

where q_k is the low-pressure gas transport quantity related to the ideal gas quantity q_0 and q_p is the high-pressure deviation.

For viscosity, these quantities are:

$$\begin{aligned}\mu_k &= \mu_0 \left(\frac{1}{G_2} + A_6 Y \right), \\ \mu_p &= \left(\frac{36.344 \times 10^{-6} (MT_c)^{1/2}}{V_c^{2/3}} \right) A_7 Y^2 G_2 \exp \left(A_8 + \frac{A_9}{T^*} + \frac{A_{10}}{T^{*2}} \right)\end{aligned}\tag{2.6}$$

where M is the molecular weight, V_c is the critical molar volume, $T^* = T/\epsilon_k$ is a dimensionless temperature scaling using the Lennard-Jones potential well depth ϵ_k , $Y = (\rho V_c)/6$, and $G_1 = (1 - 0.5Y)/(1 - Y)^3$, and $G_2 = \{A_1 [1 - \exp(-A_4 Y)]/Y + A_2 G_1 \exp(A_5 Y) + A_3 G_1\} / (A_1 A_4 + A_2 + A_3)$. The constants A_{1-10} are linear functions calculated as follows:

$$A_i = a_{i0} + a_{i1}\omega + a_{i2}\mu_r^4 + a_{i3}\kappa \quad i = 1, \dots, 10\tag{2.7}$$

where μ_r is the reduced dipole moment of the species, κ is the association factor of the species, and a_{ij} are constants (see Appendix ??).

Similarly, thermal conductivity components are given by:

$$\begin{aligned}\lambda_k &= \lambda_0 \left(\frac{1}{H_2} + B_6 Y \right), \\ \lambda_p &= \left(\frac{3.039 \times 10^{-4} (T_c/M)^{1/2}}{V_c^{2/3}} \right) B_7 Y^2 H_2 T_r^{1/2}\end{aligned}\tag{2.8}$$

where $H_2 = \{B_1 [1 - \exp(-B_4 Y)]/Y + B_2 G_1 \exp(B_5 Y) + B_3 G_1\} / (B_1 B_4 + B_2 + B_3)$ and B_{1-7} are defined as:

$$B_i = b_{i0} + b_{i1}\omega + b_{i2}\mu_r^4 + b_{i3}\kappa \quad i = 1, \dots, 7\tag{2.9}$$

where b_{ij} are constants (see Appendix ??). All species-related constants mentioned in this section can also be found in Table ??.

These high pressure corrections as derived and analyzed by Chung et al. show improved accuracy for approximating transport properties over a wide range of temperatures and pressures when compared to experimental data for a variety of species [10]. For carbon dioxide in particular,

2.2.2 Thermodynamics and Related Quantities

Modeling of thermodynamic quantities is also done through *PelePhysics* []. In a similar fashion to equation 2.5, thermodynamic properties can be broken up into an ideal gas component and a departure from ideal gas behavior:

$$q(\phi) = q_I(\phi) + q_D(\phi)\tag{2.10}$$

where ϕ is the appropriate combination of state variables involving temperature, specific volume, and pressure, q_I is the ideal state component and q_D is the departure component. These decompositions can be derived from fundamental thermodynamic relations []. For example, change in internal energy can be written as follows:

$$de = \left(\frac{\partial e}{\partial T} \right)_V dT + \left[T \left(\frac{\partial p}{\partial T} \right)_V - p \right] dV \quad (2.11)$$

substituting in the appropriate partial derivative using the SRK EoS and integrating from an ideal state reference point (v, t) to general point far from ideal conditions (V, T) yields:

$$e(V, T) - e(v, t) = e(v, T) - e(v, t) + a \left[\alpha - T \frac{\partial \alpha}{\partial T} \right] \int_v^V \frac{1}{V_m(V_m + b)} dV' \quad (2.12)$$

Simplifying the left- and right-hand side of Equation 2.12 and utilizing the choice of $v \rightarrow \infty$ for the ideal state volume [], we get:

$$e(V, T) = e(\infty, T) + a \left[\alpha - T \frac{\partial \alpha}{\partial T} \right] \int_{\infty}^V \frac{1}{V_m(V_m + b)} dV' \quad (2.13)$$

Evaluating the integral in Equation 2.13, we arrive at the final expression for the internal energy of the species described by the SRK EoS:

$$e(V, T) = e_I(T) + a \left[T \frac{\partial \alpha}{\partial T} - \alpha \right] \frac{1}{b} \ln \left(1 + \frac{b}{V_m} \right) \quad (2.14)$$

where $e_I(T) = c_v T$ is the ideal internal energy which is only dependent on temperature and $e_D(T, V) = a \left[T \frac{\partial \alpha}{\partial T} - \alpha \right] \frac{1}{b} \ln \left(1 + \frac{b}{V_m} \right)$ is the departure function for the internal energy. A similar procedure can be done to arrive at the decomposed enthalpy equation involving SRK EoS-specific quantities:

$$h(T, V) = h_I(T) + a \left[T \frac{\partial \alpha}{\partial T} - \alpha \right] \frac{1}{b} \ln \left(1 + \frac{b}{V_m} \right) + \frac{RTb}{V_m - b} - \frac{a\alpha}{V_m + b} \quad (2.15)$$

The departure function can be directly evaluated while the ideal gas portion must be approximated.

Ideal specific heat at constant volume scaled by the ideal gas constant c_{vI}/R is approximated with NASA polynomial fits [40]. These polynomial fits have the following form:

$$\psi(T) = c_{\psi,0} + c_{\psi,1}T + c_{\psi,2}T^2 + c_{\psi,3}T^3 + c_{\psi,4}T^4 + c_{\psi,5}\frac{1}{T} \quad (2.16)$$

where $c_{\psi,0-5}$ are species-specific constants for each quantity's polynomial fit (see Appendix ??). Other ideal gas quantities of interest can also be calculated in this form via integration, so that ψ

here can be either ideal internal energy e_I/RT , specific heat at constant volume c_{vI}/R , or enthalpy h_I/RT . The equations for additional thermodynamic quantities, such as constant volume and constant pressure specific heat, and useful derivatives involving the SRK EoS can be found in Appendix ??.

2.2.3 Filtered Navier-Stokes Equations

To perform the LES, we consider the filtered compressible Navier-Stokes equations as implemented by Martín, Piomelli, and Graham [38]. Here we go through a brief derivation along with the main assumptions needed. First, applying the filtering operation from Equation 1.13 to Equations 2.1, we get:

$$\frac{\partial \bar{\rho}}{\partial t} + \frac{\partial}{\partial x_j} (\bar{\rho} \bar{u}_j) = 0, \quad (2.17a)$$

$$\frac{\partial}{\partial t} (\bar{\rho} \bar{u}_i) + \frac{\partial}{\partial x_j} (\bar{\rho} \bar{u}_i \bar{u}_j + \bar{p} \delta_{ij} - \bar{\sigma}_{ij}) = 0, \quad (2.17b)$$

$$\frac{\partial}{\partial t} (\bar{\rho} \bar{E}) + \frac{\partial}{\partial x_j} ((\bar{\rho} \bar{E} \bar{u}_j + \bar{p} \bar{u}_j) + \bar{q}_j - \bar{\sigma}_{ij} \bar{u}_i) = 0 \quad (2.17c)$$

In order to avoid having to model $\bar{\rho} \bar{u}_j$ in the conservation of mass equation in 2.17, Favre-filtering, $\tilde{\cdot} = \bar{\rho} \bar{\cdot} / \bar{\rho}$, is also applied []. Additionally, the following two sets of assumptions are made regarding transport terms []:

$$\overline{\mu(T) S_{ij}} \simeq \mu(\tilde{T}) \widetilde{S_{ij}}, \quad \overline{\lambda(T) \frac{\partial T}{\partial x_j}} \simeq \lambda(\tilde{T}) \frac{\partial \tilde{T}}{\partial x_j} \quad (2.18a)$$

$$\tilde{\mu} = \mu(\tilde{T}), \quad \tilde{\lambda} = \lambda(\tilde{T}) \quad (2.18b)$$

The assumptions in Equations 2.18 are common in the literature regarding LES, even though transport terms are nonlinearly dependent on temperature []. Justification for this type of assumption can be made where if performing a LES with course enough grid, molecular transport coefficients remain small compared to turbulent transport coefficients []. Applying Equations 2.18 along with the Favre filter to Equations 2.17 yields the following:

$$\frac{\partial \bar{\rho}}{\partial t} + \frac{\partial}{\partial x_j} (\bar{\rho} \tilde{u}_j) = 0,$$

$$\frac{\partial}{\partial t} (\bar{\rho} \tilde{u}_i) + \frac{\partial}{\partial x_j} (\bar{\rho} \tilde{u}_i \tilde{u}_j + \bar{p} \delta_{ij} - \tilde{\sigma}_{ij}) = 0, \quad (2.19)$$

$$\frac{\partial}{\partial t} (\bar{\rho} \tilde{E}) + \frac{\partial}{\partial x_j} ((\bar{\rho} \tilde{E} \tilde{u}_j + \bar{p} \tilde{u}_j) + \tilde{q}_j - \tilde{\sigma}_{ij} \tilde{u}_i) = 0$$

with filtered Equations 2.2 now given by:

$$\tilde{\sigma}_{ij} = 2\tilde{\mu} \widetilde{S_{ij}} - \frac{2}{3} \tilde{\mu} \delta_{ij} \widetilde{S_{kk}}, \quad \tilde{q}_j = -\tilde{\lambda} \frac{\partial \tilde{T}}{\partial x_j} \quad (2.20)$$

Final simplifications to Equations 2.19 come from the SGS terms. The SGS stress τ_{ij} , SGS heat flux \mathcal{Q}_j , SGS turbulent diffusion $\partial \mathcal{J}_j / \partial x_j$, and SGS turbulent viscous diffusion $\partial \mathcal{D}_j / \partial x_j$ set through the following definitions []:

$$\begin{aligned}\tau_{ij} &= \bar{\rho} (\widetilde{u_i u_j} - \widetilde{u_i} \widetilde{u_j}), \\ \mathcal{Q}_j &= \bar{\rho} (\widetilde{u_j T} - \widetilde{u_j} \widetilde{T}), \\ \mathcal{J}_j &= \bar{\rho} (u_j \widetilde{u_k u_k} - \widetilde{u_j} \widetilde{u_k u_k}), \\ \mathcal{D}_j &= \bar{\rho} (\widetilde{\sigma_{ij} u_i} - \widetilde{\sigma_{ij}} \widetilde{u_i})\end{aligned}\tag{2.21}$$

After substituting the appropriate pieces of Equations 2.21 into the momentum and energy components of 2.19 and applying a few further assumptions, we can eventually get the following:

$$\frac{\partial \bar{\rho}}{\partial t} + \frac{\partial}{\partial x_j} (\bar{\rho} \widetilde{u_j}) = 0, \tag{2.22a}$$

$$\frac{\partial}{\partial t} (\bar{\rho} \widetilde{u_i}) + \frac{\partial}{\partial x_j} (\bar{\rho} \widetilde{u_i} \widetilde{u_j} + \bar{p} \delta_{ij} - \widetilde{\sigma_{ij}}) = -\frac{\partial \tau_{ij}}{\partial x_j}, \tag{2.22b}$$

$$\frac{\partial}{\partial t} (\bar{\rho} \widetilde{E}) + \frac{\partial}{\partial x_j} \left((\bar{\rho} \widetilde{E} + \bar{p}) \widetilde{u_j} + \widetilde{q_j} - \widetilde{\sigma_{ij} u_i} \right) = -\frac{\partial}{\partial x_j} \left(\gamma c_v \mathcal{Q}_j + \frac{1}{2} \mathcal{J}_j - \mathcal{D}_j \right) \tag{2.22c}$$

with $\gamma = c_p / c_v$. The simplification above hinges upon relating enthalpy to internal energy and pressure as in the ideal gas case with $h = e + p/\rho = c_p T$ with c_p assumed to be constant. Neither of these assumptions is consistent with supercritical fluids but is chosen here for ease of splitting Equations ?? into simulated vs. modeled quantities. This is also standard practice in many supercritical LES studies [], though these assumptions leave room for future work on incorporating higher order EoS into the LES derivation.

Finally, it is also noted that the divergence of the SGS heat flux and the SGS turbulent diffusion are of comparable order of magnitude while the SGS viscous diffusion is an order of magnitude smaller [38]. Therefore, the SGS turbulent viscous diffusion is omitted from the system. The final set of equations to be discretized and advanced is given by:

$$\frac{\partial \bar{\rho}}{\partial t} + \frac{\partial}{\partial x_j} (\bar{\rho} \widetilde{u_j}) = 0, \tag{2.23a}$$

$$\frac{\partial}{\partial t} (\bar{\rho} \widetilde{u_i}) + \frac{\partial}{\partial x_j} (\bar{\rho} \widetilde{u_i} \widetilde{u_j} + \bar{p} \delta_{ij} - \widetilde{\sigma_{ij}}) = -\frac{\partial \tau_{ij}}{\partial x_j}, \tag{2.23b}$$

$$\frac{\partial}{\partial t} (\bar{\rho} \widetilde{E}) + \frac{\partial}{\partial x_j} \left((\bar{\rho} \widetilde{E} + \bar{p}) \widetilde{u_j} + \widetilde{q_j} - \widetilde{\sigma_{ij} u_i} \right) = -\frac{\partial}{\partial x_j} \left(\gamma c_v \mathcal{Q}_j + \frac{1}{2} \mathcal{J}_j \right) \tag{2.23c}$$

with Equations 2.20 describing the filtered transport coefficients. The SGS stress τ_{ij} , SGS heat flux \mathcal{Q}_j , and SGS turbulent diffusion \mathcal{J}_j need to be modeled in order to close the system.

2.2.4 Subgrid-Scale Modeling for Large Eddy Simulation

We use the SMD LES model for compressible flow as described by Martín, Piomelli, and Graham [38]. In this work, the grid provides the implicit filtering of the equations. The SGS stress tensor, τ_{ij} , is included in the diffusive fluxes and is calculated as follows:

$$\begin{aligned}\tau_{ij} - \frac{\delta_{ij}}{3}\tau_{kk} &= -C_s^2 2\bar{\Delta}^2 \bar{\rho} |\tilde{S}| \left(\tilde{S}_{ij} - \frac{\delta_{ij}}{3}\tilde{S}_{kk} \right) = C_s^2 \alpha_{ij}, \\ \tau_{kk} &= C_I 2\bar{\rho} \bar{\Delta}^2 |\tilde{S}|^2 = C_I \alpha\end{aligned}\quad (2.24)$$

with $\bar{\Delta}$ being the filter width associated with the smallest scale retained by the filtering operation ($\bar{\Delta}$ is the grid spacing for our cases). Additionally, $|\tilde{S}| = (2\tilde{S}_{ij}\tilde{S}_{ij})^{1/2}$. The two model coefficients are calculated as follows:

$$C = C_s^2 = \frac{\langle \mathcal{L}_{ij} M_{ij} \rangle}{\langle M_{kl} M_{kl} \rangle}, \quad C_I = \frac{\langle \mathcal{L}_{kk} \rangle}{\langle \beta - \hat{\alpha} \rangle} \quad (2.25)$$

where the Germano identity, $\mathcal{L}_{ij} = T_{ij} - \hat{\tau}_{ij}$, is used to relate the SGS stress tensor to the “resolved turbulent stresses”, $\mathcal{L}_{ij} = \left(\overline{\rho u_i \widehat{\rho u_j}} / \bar{\rho} \right) - \widehat{\rho u_i \widehat{\rho u_j}} / \hat{\rho}$, and the subtest stresses, $T_{ij} = \widehat{\rho \check{u}_i \check{u}_j} - \widehat{\rho \check{u}_i} \check{u}_j$ [21]. In this relationship, a hat denotes quantities associated with a test filter \hat{G} which has a characteristic length of $\hat{\Delta}$. The breve denotes Favre-filtered quantities using \hat{G} (i.e., $\check{f} = \widehat{\rho f / \bar{\rho}}$). Additionally, $M_{ij} = \beta_{ij} - \hat{\alpha}_{ij}$ with $\beta_{ij} = -2\hat{\Delta}^2 \hat{\rho} |\check{S}| \left(\check{S}_{ij} - \delta_{ij} \check{S}_{kk} / 3 \right)$ and $\beta = 2\hat{\Delta}^2 \hat{\rho} |\check{S}|^2$.

The SGS heat flux \mathcal{Q}_j is also modeled dynamically as in [38]:

$$\mathcal{Q}_j = -\frac{\bar{\rho} \nu_T}{Pr_T} \frac{\partial \tilde{T}}{\partial x_j} = -C \frac{\bar{\Delta}^2 \bar{\rho} |\tilde{S}|}{Pr_T} \frac{\partial \tilde{T}}{\partial x_j} \quad (2.26)$$

where C is modeled as in Equation 2.25 and the turbulent Prandtl number, Pr_T , is calculated dynamically as:

$$Pr_T = \frac{C \langle T_k T_k \rangle}{\langle \mathcal{K}_j T_j \rangle} \quad (2.27)$$

where

$$T_j = -\hat{\Delta}^2 \hat{\rho} |\check{S}| \frac{\partial \check{T}}{\partial x_j} + \bar{\Delta}^2 \bar{\rho} |\tilde{S}| \frac{\partial \tilde{T}}{\partial x_j}, \quad \mathcal{K}_j = \left(\frac{\widehat{\rho u_j \rho \tilde{T}}}{\bar{\rho}} \right) - \frac{\widehat{\rho u_j} \hat{\rho \tilde{T}}}{\hat{\rho}}. \quad (2.28)$$

Finally, the SGS turbulent diffusion \mathcal{J}_j is modeled following the strategy proposed by Knight et al. [1]:

$$\mathcal{J}_j = \tilde{u}_k \tau_{jk} \quad (2.29)$$

For our simulations, we implement the three point box filter as described in [53] with a filter-grid ratio of 2, i.e. $\hat{\Delta} = 2\bar{\Delta}$. With this filter, the convolution kernel from Equation 1.13 is defined as

follows:

$$G(\mathbf{x} - \mathbf{r}) = \begin{cases} \frac{1}{\hat{\Delta}} & |\mathbf{x} - \mathbf{r}| \leq \frac{\hat{\Delta}}{2}, \\ 0 & \text{otherwise} \end{cases} \quad (2.30)$$

The discrete implementation of this filtering function is described in the numerical methods section.

As noted previously, the choice of SGS modeling is important in accurately capturing the turbulence statistics of the system. Müller et al. found that while the choice in thermodynamic modeling is crucial in capturing first-order moments, the effects SGS modeling is limited to second-order moments [42]. Therefore, our conclusions relating to the turbulence dynamics will be unaffected. That being said, [42] also notes that the choice in SGS model and numerical flux discretization had a larger than expected effect on resolved Reynolds stress profiles. Specifically, the constant Smagorinsky model yielded decaying fluctuation magnitudes during early evolution, resulting in the transition to a fully turbulent mixing zone to start from lower turbulence levels. However, this did agree with the jet break-up location inferred from mean density profiles, which were shifted slightly downstream by comparison to other SGS models. These relationships will be taken into consideration for this study as well and noted in the discussion of Reynolds stress profiles.

2.3 Validation

Make plots to compare with NIST data.

CHAPTER 3

ALGORITHM OVERVIEW

3.1 Introduction

Make one of those little flow chart thingys for overall algorithm procedure (minus meshing aspects).

3.2 Numerical Methods

3.2.1 Piecewise Parabolic Method Overview

3.2.2 Approximate Riemann Solver Details

3.3 Error

CHAPTER 4

SIMULATIONS

4.1 Computational Domain

4.1.1 AMReX and Discretization

Our target simulation is a 3D LES with a grid size that is 100 times the smallest scale of the turbulent flow. In our setup, the domain length in each direction is: $x = 25d$, $y = 62.5d$, and $z = 25d$, where the jet diameter $d = 0.01$ cm and the y -axis is the axial direction of the jet. This smallest scale of these turbulent flows, known as the Kolmogorov scale [29], can be approximated:

$$\eta = \left(\frac{\nu^3}{\varepsilon} \right) \quad (4.1)$$

where $\nu = \mu/\rho$ is the kinematic viscosity and $\varepsilon = v_j^3/d$ is used to approximate the average rate of dissipation of turbulence kinetic energy per unit mass. For these turbulent jets, $\eta = 5.37 \times 10^{-6}$ cm. Therefore, to keep the calculation tractable and achieve an adequate LES grid size, we implement four levels of refinement, with a refinement ratio of 2, leading to 80, 200, and 80 cells on the coarsest level in the x , y , and z directions, respectively. This results in an initial mesh size of $\Delta x_0 = \Delta y_0 = \Delta z_0 = 0.3125$, leading to $\Delta x_3 = \Delta y_3 = \Delta z_3 = 3.9062 \times 10^{-4}$, where the subscript denotes the AMR level. These four levels of refinement occur in the region outward from the jet inlet up to a distance of $20d$ in the x and z direction and $60d$ in the y direction, as can be seen in Figure 4.1. The refinement criterion is given by the vorticity, specifically with $\omega \geq 5000^{2l}$, where ω is the magnitude of the vorticity and l is the AMR level. For the first ten flow throughs of the simulation, mesh refinement only occurs up to one level within the refinement region to establish the flow pattern. Thereafter, the simulation proceeds with the four levels of mesh refinement until reaching steady state, whereupon statistics are collected for analysis.

4.1.2 Initial and Boundary Conditions

Our inlet consists of an opening centered in the xz -plane with diameter $d = 0.01$ cm through which the sCO₂ jet is initialized. The pressure in the jet at the inlet is the same as that of the quiescent background fluid and it is given by $p_j = p_0 = 10.1325$ MPa. The ambient fluid remains at rest while the jet is initialized with an inflow velocity of $v_j = 1800$ cm s⁻¹, leading to a Reynolds

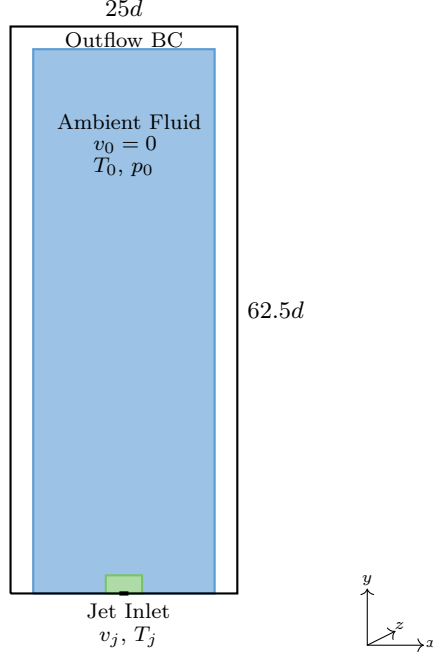


Figure 4.1: Two dimensional slice schematic of jet setup. Four levels of refinement are enforced within the green box based on proximity to jet inlet. Refinement based on vorticity criterion then occurs within the blue region. Outside the blue region, AMR is explicitly turned off to allow flow structures to be dissipated numerically and allowed to leave the domain without incurring spurious reflections.

number of the initialized jet of $Re_j = 22910$, with v_j and d being the reference velocity and length scale respectively. For the jet temperature and pressure conditions given, the reference density is $\rho_j = 3.019 \times 10^{-1} \text{ g cm}^{-3}$, as calculated via the SRK EoS in *PeleC*. To implement a turbulent inflow, we add noise to this input velocity using the mean velocity and root mean square (rms) values from a predetermined DNS velocity profile [17]. We begin by scaling the DNS values with our given jet velocity and radius. After determining which scaled DNS values we are near for the radius determined by our mesh, a linear interpolant is created to compute the mean velocity at our given radius. Noise is then added to each cylindrical component of the velocity as follows:

$$v = \langle v_{\text{DNS}} \rangle + (v'_{\text{DNS}} + \beta v'_{\text{DNS}} r_1 \sin \theta_1) \cdot r_2 \sin \theta_2 \quad (4.2a)$$

$$u = u'_{\text{DNS}} + \beta u'_{\text{DNS}} r_3 \sin \theta_3 \quad (4.2b)$$

$$w = w'_{\text{DNS}} + \beta w'_{\text{DNS}} r_4 \sin \theta_4 \quad (4.2c)$$

where $\langle u_y \rangle$ is the mean velocity in the axial direction, $u' = \langle u^2 \rangle^{\frac{1}{2}}$ is the rms for each velocity component, and $\beta = 0.1$. Each r_i and θ_k value is randomly generated as follows:

$$r_i = \sqrt{-2.0 \log(X_i)} \quad (4.3a)$$

$$\theta_k = 2\pi X_k \quad (4.3b)$$

where X_n are random numbers between 0 and 1. The inflow parameters are finalized after being converted into Cartesian coordinates.

We implement zero gradient boundary conditions for all boundaries not involving the jet inflow. Additionally, AMR is halted at a distance of $2.5d$ from the boundary in the x and z directions, and that of $5d$ in the axial direction in order to ensure that all waves are dissipated, thus avoiding spurious reflections from the boundaries.

4.2 Case Descriptions

4.2.1 Parameter Choices

4.3 Compute Time and Hardware Specifications

4.4 Post-Processing Procedures

CHAPTER 5

RESULTS

5.1 Isothermal Jet

Our first case involves the isothermal jet where both jet and ambient fluid are at $330K$. Quantities of interest for this case are compared against incompressible round jet statistics as outlined in Pope [46] and isothermal compressible jet turbulence features []. This case serves as a baseline for comparison with the other two cases involving non-isothermal jets.

5.1.1 Flow Field Features

All images herein depict a slice of the 3D flow field at $z = 0$. Each figure contains an instantaneous snapshot and a time-averaged snapshot of the entire slice domain, plus an additional zoomed-in image of the time-averaged quantity of interest near the inlet. All instantaneous images are taken from the final data point of the simulation.

Figure 5.1 shows the axial velocity component of the flow field. The general spreading rate and decay of the velocity field can be seen from the instantaneous snapshot in 5.1a. The flow is mostly steady up until $y/d = 2$ before perturbations begin. The stream mostly stays together through these initial perturbations up until $y/d = 5$ where spreading then begins. The averaged axial velocity fields in 5.1b and 5.1c shed more light on the approximate development regions of the jet. The potential core extends up to $y/d = 5$, followed by the transition region where $5 \leq y/d \leq 15$, thereafter the jet appears fully developed. Centerline analysis of the turbulent kinetic energy later on will provide more information for these boundaries.

Figure 5.2 shows minor pressure fluctuations in the flow, scaled against the maximum pressure achieved above the ambient pressure. 5.2a shows minor pressure oscillations mirrored on each side of the jet edge in the same way as the initial velocity fluctuations see in 5.1a. Thereafter, the oscillations become off-kilter, correlating to the beginning of the jet disintegration as seen in the velocity field. Pressure fluctuations are concentrated near the inlet and die down past the transition zone. This can be seen more clearly in 5.2b. On average, pressure fluctuations yield a minor increase within the potential core and decrease on the jet perimeter, as can be seen in 5.2c. Fluctuations also lead to a minor pressure drop on average in the transition region.

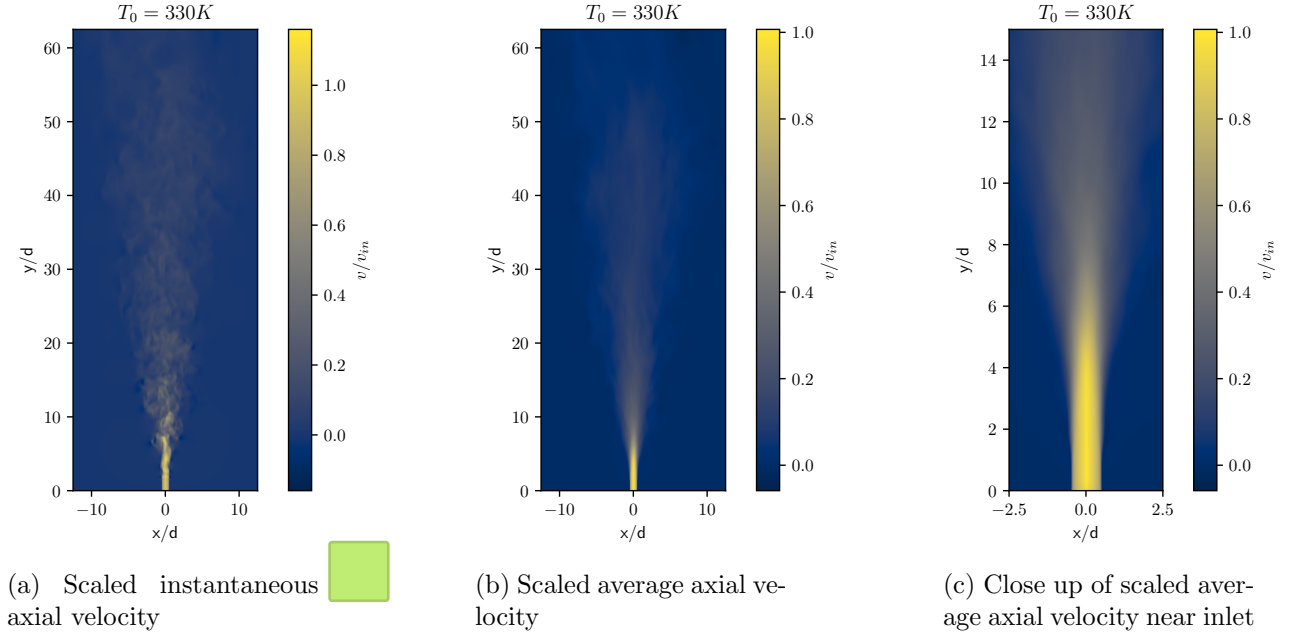


Figure 5.1: Axial velocity features of the isothermal jet

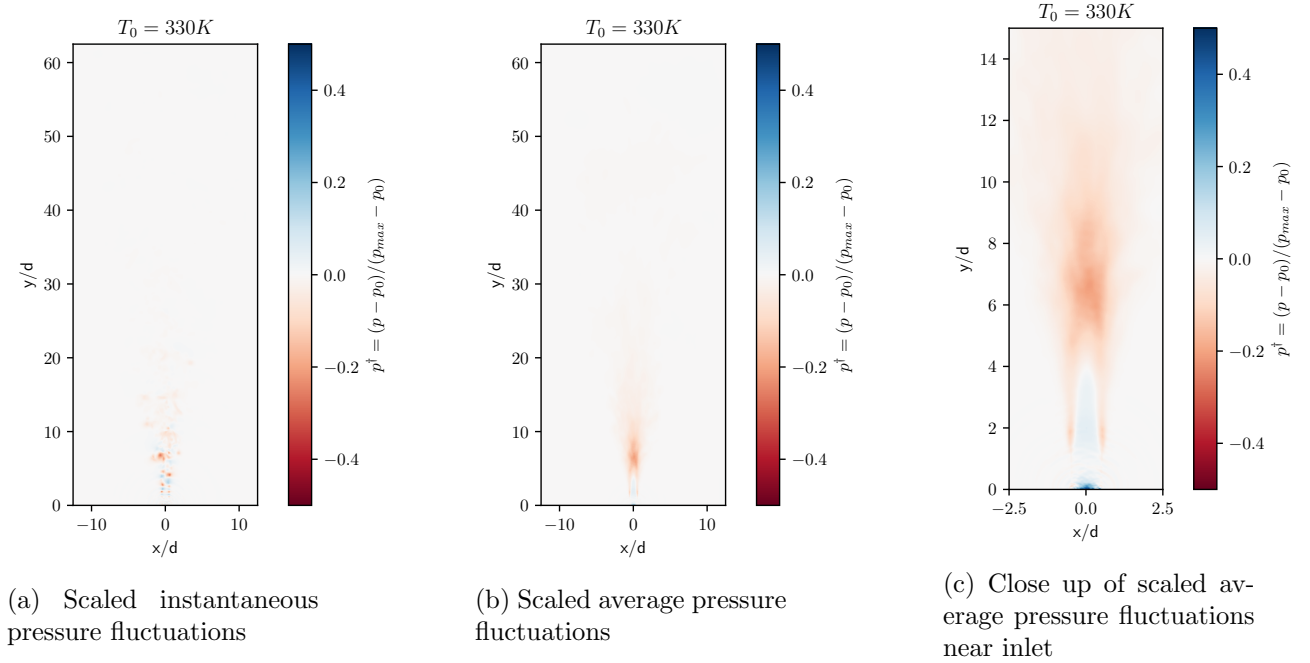


Figure 5.2: Pressure features of the isothermal jet

Figure 5.3 shows magnitude of the vorticity scaled between the maximal and minimal values. 5.3a shows the strongest vorticity occurring at the jet interface with the ambient fluid near the inlet. Past this initial stage, vortex shedding occurs and vorticity dissipates as the jet spreads. The averages in 5.3b and 5.3c both show again that the most intense vorticity occurs at the inlet along the outer edge of the jet. This high intensity remains constant until about $y/d = 1$ before more mixing with the ambient fluid occurs as the jet spreads and the vorticity lessens in intensity. Vortices are still restricted to the jet edge until around $y/d = 5$ where the transition to fully developed turbulence enables vortical motions to extend across the fully spread of the jet.

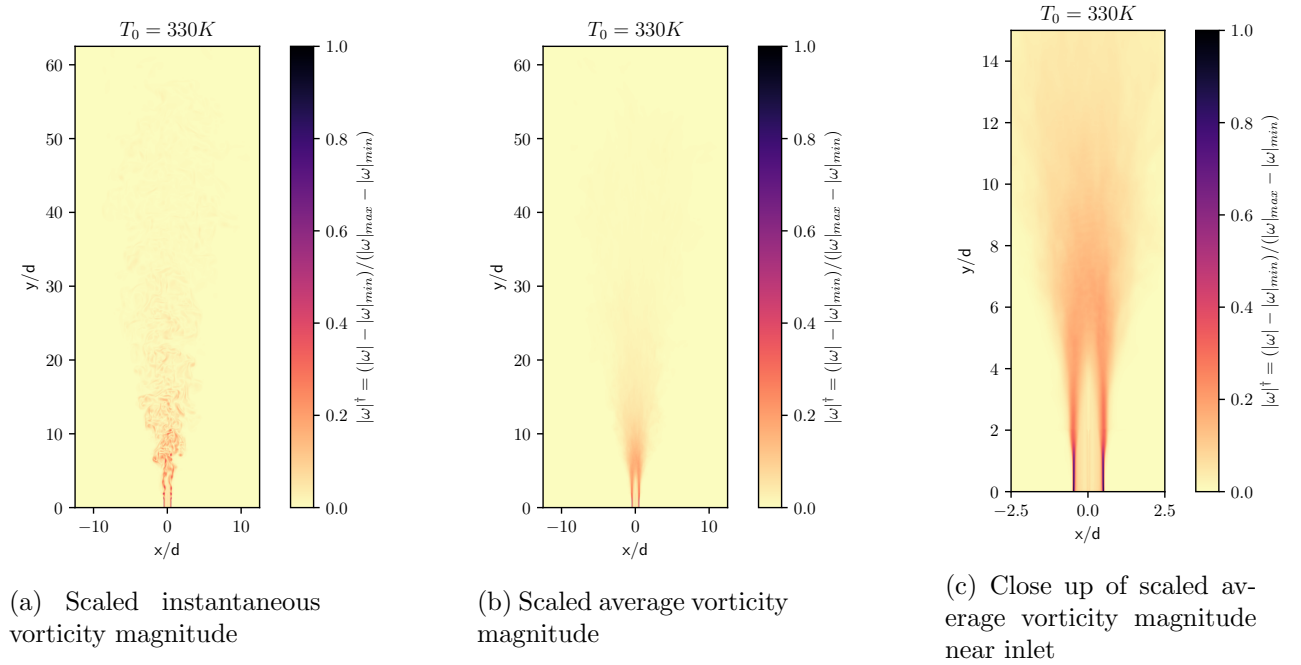


Figure 5.3: Vorticity magnitude features of the isothermal jet

5.1.2 Mean Flow Properties

Figure 5.4 depicts the time and radially averaged scaled axial velocity component plotted against radial distance from the centerline at multiple normal slices downstream from the inlet. The velocity is scaled by the average axially velocity value at the inflow while the radial direction is scaled by the jet diameter. These plots demonstrate the axially velocity decay as the flow progresses further downstream. As velocity value along the centerline decreases, the overall velocity profile expands and flattens out. Typically, for the round turbulent jet, this expansion would occur in such a way

that upon specially selected scaling, these profiles would collapse into one profile after a certain point. This potential is explored further in the next figure. ~~Here though~~ this decay is a common feature of how the axial velocity of the jet develops as it leaves the inlet.

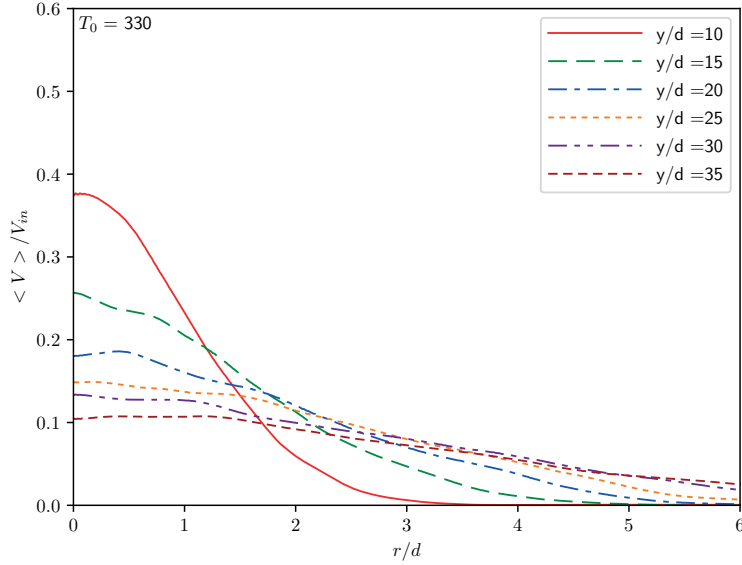


Figure 5.4: Average (both in time and radially) axial velocity scaled by inlet value plotted along radial distance from centerline. Profile decay follows similar trajectory to what is expected in incompressible round jet theory [46].

Figure 5.5 depicts time and radially averaged scaled axial velocity components plotted against the radial distance from the centerline. Each curve is made at a slice normal to the axial flow direction at different points downstream. Figure 5.5a depicts velocity curves every $3d$ downstream from the inlet near where the transition region begins while Figure 5.5b contains plots taken every $5d$. The axial velocity is scaled by the centerline value v_c while the radial distance is scaled by the half width half mean (HWHM), where the velocity component is equal to half the value on the centerline $v(r_{1/2}) = v_c/2$.

Figure 5.5a shows the near-field axial velocity profiles. They ~~collapse~~ exhibit self-similarity collapse into one profile which is most likely the result of the inflow condition []. In the far-field slices of 5.5b, self-similarity is fairly well maintained with minor fluctuations in the center and edge of the jet. These fluctuations are most likely the result of low resolution in the time averaging of available data.

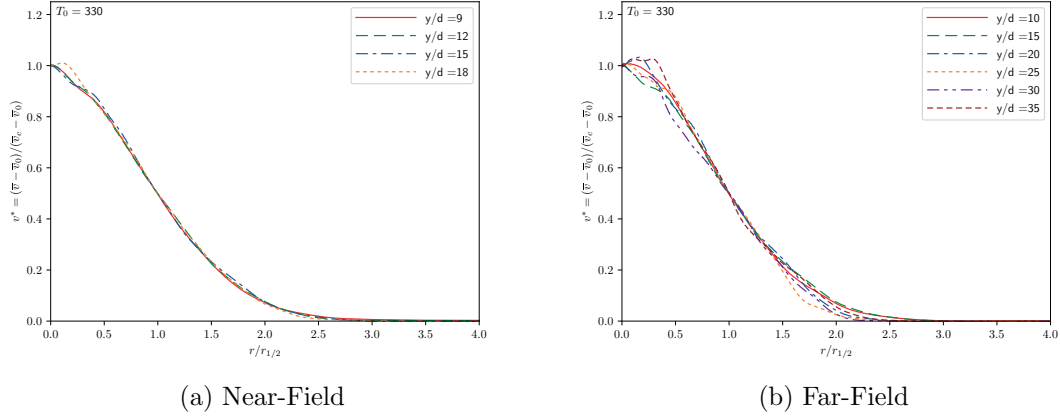


Figure 5.5: Normal slices of scaled axial velocity, averaged in both time and the radial direction. Plotted against radial direction scaled by $r_{1/2}$. Both near- and far-field regions demonstrate the self-similarity within the round turbulent jet.

Another common feature of round turbulent jets is the development of a linear relationship between the jet centerline value and the distance downstream. This comparison is depicted in Figure 5.6. Here, the centerline value of the axial velocity v_0 is inversely linearly proportional to the distance downstream. The dip at $y/d = 30$ may be attributed to again lack of convergence due to low sample size in time averaging.

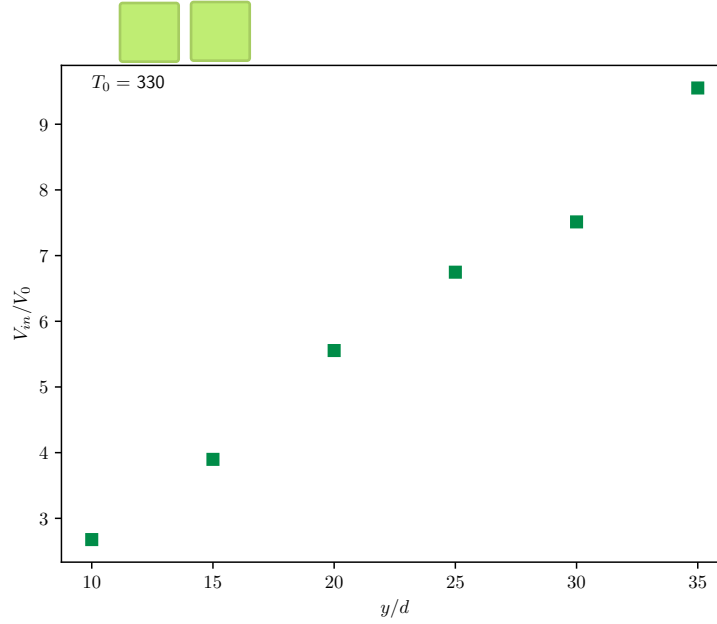
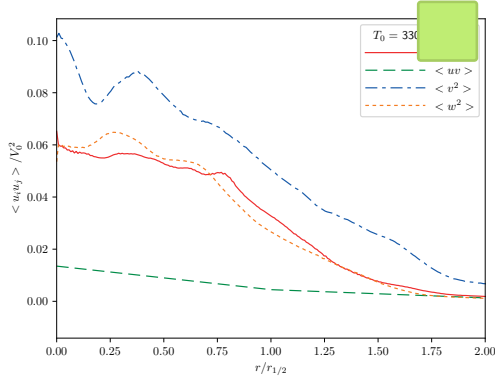


Figure 5.6: Axial inlet velocity scaled by centerline values along the axial direction. When distance downstream is scaled by jet diameter, linear decay of the centerline axial velocity is observed.

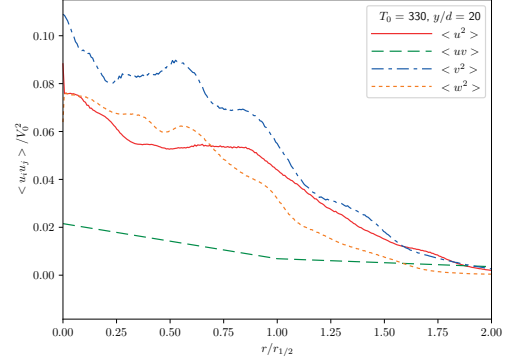
5.1.3 Turbulence Dynamics

Figure 5.7 shows the time and radially averaged Reynolds stresses at two points downstream from the inlet. Here, velocity components (u, v, w) correspond to the (r, y, θ) directions, respectively. Each Reynolds stress component follows general trends associated with round turbulent jets [46], with the axial component providing the leading contribution, followed by the other two directional components closely with these two being of roughly the same magnitude, and the cross-directional component contributing the least. The cross-directional component is non-zero at the jet center; this could be due to... Note also that self-similarity is not exhibited, as each component exhibits an increase in magnitude at the center of the jet as distance downstream is increased.

Figure 5.8 shows the time average turbulent kinetic energy components along the centerline of the jet. Each component grows through the potential core region of the jet up until all components reach a peak in energy around $y/d = 6$, with the axial component's peak coming slightly ahead of the other two directions. Rapid decay is then observed up until around $y/d = 15$ before a slower decay sets in up until a leveling off is achieved around $y/d = 30$. This rapid decay and then further progression correspond to the transition and fully developed jet regions, respectively.



(a) Reynolds stresses at $y/d = 15$



(b) Reynolds stresses at $y/d = 20$

Figure 5.7: Time and radially averaged Reynolds stresses for the isothermal jet at two locations downstream. Both slices follow similar Reynolds stress relations as seen in incompressible round jet [46].

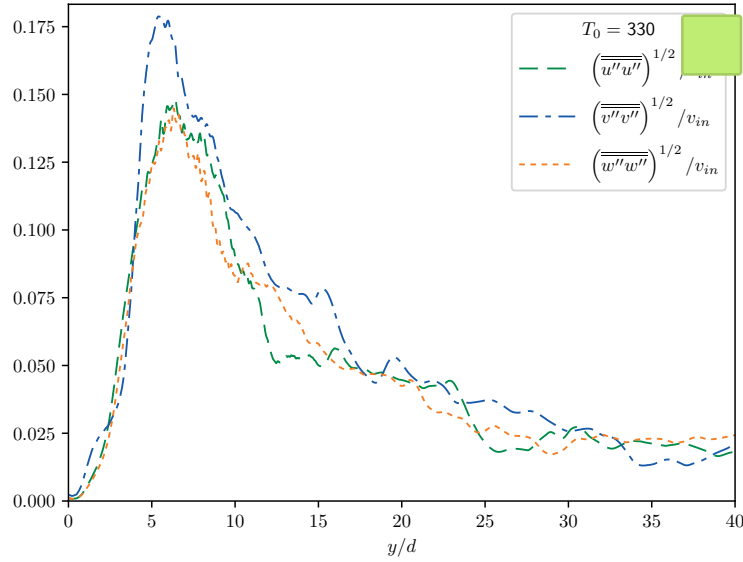


Figure 5.8: Average turbulent kinetic energy components along centerline.

5.2 Non-Isothermal Jets

5.2.1 Flow Field Features

5.2.2 Mean Flow Properties

5.2.3 Turbulence Dynamics

5.3 Discussion

CHAPTER 6

CONCLUSION

- 6.1 Summary
- 6.2 Future Work

APPENDIX A

TRANSPORT COEFFICIENTS

A.1 EGLib Low Pressure Approximation Coefficients

A.2 Chung High Pressure Correction Coefficients

Chung et al. [10] details the derivation of these general transport coefficients via their regression analysis of various fluids. The coefficients for the linear approximation are printed here for convenience as they are implemented in *PelePhysics* [].

Table A.1: Linear Coefficients Used in Calculating High Pressure Viscosity Corrections as found by Chung et al. [10]

i	a_{i0}	a_{i1}	a_{i2}	a_{i3}
1	6.32402	50.41190	-51.68010	1189.02000
2	$0.121\,02 \times 10^{-2}$	$-0.115\,36 \times 10^{-2}$	$-0.625\,71 \times 10^{-2}$	$0.372\,83 \times 10^{-1}$
3	5.28346	254.20900	-168.48100	3898.27000
4	6.62263	38.09570	-8.46414	31.41780
5	19.74540	7.63034	-14.35440	31.52670
6	-1.89992	-12.53670	4.98529	-18.15070
7	24.27450	3.44945	-11.29130	69.34660
8	0.79716	1.11764	$0.123\,48 \times 10^{-1}$	-4.11661
9	-0.23816	$0.676\,95 \times 10^{-1}$	-0.81630	4.02528
10	$0.686\,29 \times 10^{-1}$	0.34793	0.59256	-0.72663

Table A.2: Linear Coefficients Used in Calculating High Pressure Thermal Conductivity Corrections as found by Chung et al. [10]

i	b_{i0}	b_{i1}	b_{i2}	b_{i3}
1	2.41657	0.74824	-0.91858	121.72100
2	-0.50924	-1.50936	-49.99120	69.98340
3	6.61069	5.62073	64.75990	27.03890
4	14.54250	-8.91387	-5.63794	74.34350
5	0.79274	0.82019	-0.69369	6.31734
6	-5.86340	12.80050	9.58926	-65.52920
7	81.17100	114.15800	-60.84100	466.77500

APPENDIX B

ADDITIONAL THERMODYNAMIC QUANTITIES

B.1 Ideal Gas NASA Polynomial Fit Coefficients

B.2 SRK Derivatives

Chung et al. [10] details the derivation of these general transport coefficients via their regression analysis of various fluids. The coefficients for the linear approximation are printed here for convenience as they are implemented in *PelePhysics* [].

Table B.1: Linear Coefficients Used in Calculating High Pressure Viscosity Corrections as found by Chung et al. [10]

i	a_{i0}	a_{i1}	a_{i2}	a_{i3}
1	6.32402	50.41190	-51.68010	1189.02000
2	$0.121\,02 \times 10^{-2}$	$-0.115\,36 \times 10^{-2}$	$-0.625\,71 \times 10^{-2}$	$0.372\,83 \times 10^{-1}$
3	5.28346	254.20900	-168.48100	3898.27000
4	6.62263	38.09570	-8.46414	31.41780
5	19.74540	7.63034	-14.35440	31.52670
6	-1.89992	-12.53670	4.98529	-18.15070
7	24.27450	3.44945	-11.29130	69.34660
8	0.79716	1.11764	$0.123\,48 \times 10^{-1}$	-4.11661
9	-0.23816	$0.676\,95 \times 10^{-1}$	-0.81630	4.02528
10	$0.686\,29 \times 10^{-1}$	0.34793	0.59256	-0.72663

Table B.2: Linear Coefficients Used in Calculating High Pressure Thermal Conductivity Corrections as found by Chung et al. [10]

i	b_{i0}	b_{i1}	b_{i2}	b_{i3}
1	2.41657	0.74824	-0.91858	121.72100
2	-0.50924	-1.50936	-49.99120	69.98340
3	6.61069	5.62073	64.75990	27.03890
4	14.54250	-8.91387	-5.63794	74.34350
5	0.79274	0.82019	-0.69369	6.31734
6	-5.86340	12.80050	9.58926	-65.52920
7	81.17100	114.15800	-60.84100	466.77500

BIBLIOGRAPHY

- [1] Salonika Aggarwal and Marko Hakovirta. “Supercritical Carbon dioxide: Adequately Sole Solvent.” In: *American Journal of Engineering, Science and Technology* 10 (2021), pp. 46–61. URL: <https://journalsonline.org/american-journal-of-engineering-science-and-technology/pdfs/volume-10/4.pdf>.
- [2] *Numerical research of the influence of the geometric parameters of shadowing fins on the intensity of jet cooling by supercritical carbon dioxide*. Vol. 1683. Journal of Physics: Conference Series. 2020. DOI: [doi:10.1088/1742-6596/1683/2/022050](https://doi.org/10.1088/1742-6596/1683/2/022050). URL: <https://iopscience.iop.org/article/10.1088/1742-6596/1683/2/022050/pdf>.
- [3] Abdulaziz Alkandari and Alexander S. Rattner. “Characterization of laminar and turbulent supercritical carbon dioxide slot jet impingement heat transfer.” In: *International Journal of Heat and Mass Transfer* 193 (2022), p. 122949. ISSN: 0017-9310. DOI: <https://doi.org/10.1016/j.ijheatmasstransfer.2022.122949>. URL: <https://www.sciencedirect.com/science/article/pii/S0017931022004227>.
- [4] Rodney John Allam, Miles Palmer, Glenn William Brown, et al. *System and method for high efficiency power generation using a carbon dioxide circulating working fluid*. US Patent 8,596,075. Dec. 2013.
- [5] Rodney Allam et al. “Demonstration of the Allam Cycle: An Update on the Development Status of a High Efficiency Supercritical Carbon Dioxide Power Process Employing Full Carbon Capture.” In: *Energy Procedia* 114 (2017). 13th International Conference on Greenhouse Gas Control Technologies, GHGT-13, 14-18 November 2016, Lausanne, Switzerland, pp. 5948–5966. ISSN: 1876-6102. DOI: <https://doi.org/10.1016/j.egypro.2017.03.1731>. URL: <https://www.sciencedirect.com/science/article/pii/S187661021731932X>.
- [6] D.T. Banuti. “Crossing the Widom-line - Supercritical pseudo-boiling.” In: *The Journal of Supercritical Fluids* 98 (2015), pp. 12–16. ISSN: 0896-8446. DOI: <https://doi.org/10.1016/j.supflu.2014.12.019>. URL: <https://www.sciencedirect.com/science/article/pii/S0896844614004306>.
- [7] R. Benzi and U. Frisch. “Turbulence.” In: *Scholarpedia* 5.3 (2010). revision #137205, p. 3439. DOI: [10.4249/scholarpedia.3439](https://doi.org/10.4249/scholarpedia.3439).
- [8] Can Cai et al. “The Flow Characteristics of Supercritical Carbon Dioxide (SC-CO₂) Jet Fracturing in Limited Perforation Scenarios.” In: *Energies* 13.10 (2020). ISSN: 1996-1073. DOI: [10.3390/en13102627](https://doi.org/10.3390/en13102627). URL: <https://www.mdpi.com/1996-1073/13/10/2627>.
- [9] Wen Chan et al. “Exergoeconomic analysis and optimization of the Allam cycle with liquefied natural gas cold exergy utilization.” In: *Energy Conversion and Management* 235 (2021), p. 113972. ISSN: 0196-8904. DOI: <https://doi.org/10.1016/j.enconman.2021.113972>. URL: <https://www.sciencedirect.com/science/article/pii/S0196890421001485>.

- [10] T.H. Chung et al. “Generalized multiparameter correlation for nonpolar and polar fluid transport properties.” In: *Ind. Eng. Chem. Res.* 27 (1988), pp. 671–679.
- [11] P. Colella and Paul R. Woodward. “The Piecewise Parabolic Method (PPM) for Gas-Dynamical Simulations.” In: *Journal of Computational Physics* 54 (Sept. 1984), pp. 174–201. DOI: [10.1016/0021-9991\(84\)90143-8](https://doi.org/10.1016/0021-9991(84)90143-8).
- [12] Phillip Colella and Michael D. Sekora. “A limiter for PPM that preserves accuracy at smooth extrema.” In: *Journal of Computational Physics* 227.15 (2008), pp. 7069–7076. ISSN: 0021-9991. DOI: <https://doi.org/10.1016/j.jcp.2008.03.034>. URL: <http://www.sciencedirect.com/science/article/pii/S0021999108001435>.
- [13] Francesco Crespi et al. “Supercritical carbon dioxide cycles for power generation: A review.” In: *Applied Energy* 195 (2017), pp. 152–183. ISSN: 0306-2619. DOI: <https://doi.org/10.1016/j.apenergy.2017.02.048>. URL: <http://www.sciencedirect.com/science/article/pii/S0306261917301915>.
- [14] Edward Dodge. *Supercritical Carbon Dioxide Power Cycles Starting to Hit the Market*. <https://breakingenergy.com/2014/11/24/supercritical-carbon-dioxide-power-cycles-starting-to-hit-the-market/>. Accessed: 2019-08-08. 2014.
- [15] Emad Dokhaee et al. “Simulation of the Allam cycle with carbon dioxide working fluid and comparison with Brayton cycle.” In: *International Journal of Energy and Environmental Engineering* 12.3 (2021), pp. 543–550. DOI: [10.1007/s40095-021-00401-4](https://doi.org/10.1007/s40095-021-00401-4). URL: <https://doi.org/10.1007/s40095-021-00401-4>.
- [16] V. Dostal, M.J. Driscoll, and P. Hejzlar. “A Supercritical Carbon Dioxide Cycle for Next Generation Nuclear Reactors.” PhD thesis. MIT, 2004.
- [17] J. G. M. Eggels et al. “Fully developed turbulent pipe flow: a comparison between direct numerical simulation and experiment.” In: *Journal of Fluid Mechanics* 268 (1994), 175?210. DOI: [10.1017/S002211209400131X](https://doi.org/10.1017/S002211209400131X).
- [18] Alexandre Ern and Vincent Giovangigli. “Fast and Accurate Multicomponent Transport Property Evaluation.” In: *Journal of Computational Physics* 120.1 (1995), pp. 105–116. ISSN: 0021-9991. DOI: <https://doi.org/10.1006/jcph.1995.1151>. URL: <https://www.sciencedirect.com/science/article/pii/S0021999185711515>.
- [19] *Explore, use, make the most of supercritical fluids*. <http://www.supercriticalfluid.org/Supercritical-fluids.146.0.html>. Accessed: 2019-08-08. 2009.
- [20] Dan Fernandes et al. “Process and Carbon Footprint Analyses of the Allam Cycle Power Plant Integrated with an Air Separation Unit.” In: *Clean Technologies* 1.1 (2019), pp. 325–340. ISSN: 2571-8797. DOI: [10.3390/cleantechnol1010022](https://doi.org/10.3390/cleantechnol1010022). URL: <https://www.mdpi.com/2571-8797/1/1/22>.

- [21] M. Germano. “Turbulence: the filtering approach.” In: *Journal of Fluid Mechanics* 238 (1992), 325–336. DOI: [10.1017/S0022112092001733](https://doi.org/10.1017/S0022112092001733).
- [22] Mehdi Ghanbari, Mahdi Ahmadi, and Asghar Lashanizadegan. “A comparison between Peng-Robinson and Soave-Redlich-Kwong cubic equations of state from modification perspective.” In: *Cryogenics* 84 (2017), pp. 13–19. ISSN: 0011-2275. DOI: <https://doi.org/10.1016/j.cryogenics.2017.04.001>. URL: <https://www.sciencedirect.com/science/article/pii/S0011227516303538>.
- [23] R. P. Gordon. “A supercritical phase separation: The gas-gas equilibrium.” In: *Journal of Chemical Education* 49.4 (1972), p. 249. DOI: [10.1021/ed049p249](https://doi.org/10.1021/ed049p249). eprint: <https://doi.org/10.1021/ed049p249>. URL: <https://doi.org/10.1021/ed049p249>.
- [24] Marc T Henry de Frahan et al. “PeleC: An adaptive mesh refinement solver for compressible reacting flows.” In: *The International Journal of High Performance Computing Applications* 0.0 (2022), p. 10943420221121151. DOI: [10.1177/10943420221121151](https://doi.org/10.1177/10943420221121151). URL: <https://doi.org/10.1177/10943420221121151>.
- [25] Man Huang et al. “Analysis of the flow characteristics of the high-pressure supercritical carbon dioxide jet.” In: *Journal of Hydrodynamics* 31 (2019), pp. 389–399. DOI: <https://doi.org/10.1007/s42241-018-0165-8>. URL: <https://link.springer.com/article/10.1007/s42241-018-0165-8#citeas>.
- [26] Man Huang et al. “Experimental investigation on the flow and rock breaking characteristics of supercritical carbon dioxide jets.” In: *Journal of Petroleum Science and Engineering* 187 (2020), p. 106735. ISSN: 0920-4105. DOI: <https://doi.org/10.1016/j.petrol.2019.106735>. URL: <https://www.sciencedirect.com/science/article/pii/S0920410519311544>.
- [27] Nikolaos D. Katopodes. “Chapter 1 - Basic Concepts.” In: *Free-Surface Flow*. Ed. by Nikolaos D. Katopodes. Butterworth-Heinemann, 2019, pp. 2–98. ISBN: 978-0-12-815489-2. DOI: <https://doi.org/10.1016/B978-0-12-815489-2.00001-0>. URL: <https://www.sciencedirect.com/science/article/pii/B9780128154892000010>.
- [28] Imane Ghaleb Khalil. “Free-Jet Expansion of Supercritical CO₂.” PhD thesis. University of California, San Diego, 2003.
- [29] A. Kolmogorov. “The Local Structure of Turbulence in Incompressible Viscous Fluid for Very Large Reynolds’ Numbers.” In: *Akademiia Nauk SSSR Doklady* 30 (Jan. 1941), pp. 301–305.
- [30] A. V. Lazarev and K. A. Tatarenko. “Gas dynamic model of the expansion of a supercritical carbon dioxide pulse jet: A self-similar solution.” In: *Russian Journal of Physical Chemistry B* 10.8 (2016), pp. 1248–1255. DOI: [10.1134/S1990793116080145](https://doi.org/10.1134/S1990793116080145). URL: <https://doi.org/10.1134/S1990793116080145>.

- [31] Hua-Guang Li, Xi-Yun Lu, and Vigor Yang. “A numerical study of fluid injection and mixing under near-critical conditions.” In: *Acta Mechanica Sinica* 28.3 (June 2012), pp. 559–571. ISSN: 1614-3116. DOI: [10.1007/s10409-012-0035-5](https://doi.org/10.1007/s10409-012-0035-5). URL: <https://doi.org/10.1007/s10409-012-0035-5>.
- [32] Mukun Li et al. “Comparative simulation research on the stress characteristics of supercritical carbon dioxide jets, nitrogen jets and water jets.” In: *Engineering Applications of Computational Fluid Mechanics* 11.1 (2017), pp. 357–370. DOI: [10.1080/19942060.2017.1293565](https://doi.org/10.1080/19942060.2017.1293565). eprint: <https://doi.org/10.1080/19942060.2017.1293565>. URL: <https://doi.org/10.1080/19942060.2017.1293565>.
- [33] Mukun Li et al. “Flow energy transformation and dissipation mechanisms of carbon dioxide, nitrogen, and water jets.” In: *Journal of Natural Gas Science and Engineering* 84 (2020), p. 103650. ISSN: 1875-5100. DOI: <https://doi.org/10.1016/j.jngse.2020.103650>. URL: <https://www.sciencedirect.com/science/article/pii/S1875510020305047>.
- [34] Mukun Li et al. “Influences of Supercritical Carbon Dioxide Jets on Damage Mechanisms of Rock.” In: *Arabian Journal for Science and Engineering* 43.5 (May 2018), pp. 2641–2658. ISSN: 2191-4281. DOI: [10.1007/s13369-017-2984-2](https://doi.org/10.1007/s13369-017-2984-2). URL: <https://doi.org/10.1007/s13369-017-2984-2>.
- [35] *Experimental Investigation in Turbulent Shear Mixing Layer at Supercritical Condition*. Vol. Volume 2: Multiphase Flow (MFTC); Computational Fluid Dynamics (CFDTC); Micro and Nano Fluid Dynamics (MNFDTC). Fluids Engineering Division Summer Meeting. V002T04A010. Aug. 2022. DOI: [10.1115/FEDSM2022-87029](https://doi.org/10.1115/FEDSM2022-87029). eprint: <https://asmedigitalcollection.asme.org/FEDSM/proceedings-pdf/FEDSM2022/85840/V002T04A010/6923087/v002t04a010-fedsm2022-87029.pdf>. URL: <https://doi.org/10.1115/FEDSM2022-87029>.
- [36] Yong Liu et al. “Application of supercritical carbon dioxide jet: A parametric study using numerical simulation model.” In: *Journal of Petroleum Science and Engineering* 201 (2021), p. 108422. ISSN: 0920-4105. DOI: <https://doi.org/10.1016/j.petrol.2021.108422>. URL: <https://www.sciencedirect.com/science/article/pii/S0920410521000814>.
- [37] Q Lv et al. “Numerical investigation on the expansion of supercritical carbon dioxide jet.” In: *IOP Conference Series: Materials Science and Engineering* 52.7 (Dec. 2013), p. 072011. DOI: [10.1088/1757-899x/52/7/072011](https://doi.org/10.1088/1757-899x/52/7/072011). URL: <https://doi.org/10.1088/1757-899x/52/7/072011>.
- [38] M. Martín, Ugo Piomelli, and Graham Candler. “Subgrid-Scale Models for Compressible Large-Eddy Simulations.” In: *Theoretical and Computational Fluid Dynamics* 13 (Feb. 2000), pp. 361–376.
- [39] W Mayer et al. “Raman measurements of cryogenic injection at supercritical pressure.” In: *Heat and Mass Transfer* 39.8-9 (2003), pp. 709–719.

- [40] Bonnie McBride, Michael Zehe, and Sanford Gordon. “NASA Glenn coefficients for calculating thermodynamic properties of individual species.” In: (Oct. 2002). URL: <https://ntrs.nasa.gov/api/citations/20020085330/downloads/20020085330.pdf>.
- [41] G.H. Miller and P. Colella. “A Conservative Three-Dimensional Eulerian Method for Coupled Solid-Fluid Shock Capturing.” In: *Journal of Computational Physics* 183.1 (2002), pp. 26–82. ISSN: 0021-9991. DOI: <https://doi.org/10.1006/jcph.2002.7158>. URL: <http://www.sciencedirect.com/science/article/pii/S0021999102971585>.
- [42] Hagen Müller et al. “Large-eddy simulation of nitrogen injection at trans- and supercritical conditions.” In: *Physics of Fluids* 28.1 (2016), p. 015102. DOI: [10.1063/1.4937948](https://doi.org/10.1063/1.4937948). eprint: <https://doi.org/10.1063/1.4937948>. URL: <https://doi.org/10.1063/1.4937948>.
- [43] Syed Mohammad Ovais. “Direct Numerical Simulation of supercritical CO₂ mixing and combustion.” PhD thesis. Clemson University, 2022. URL: https://tigerprints.clemson.edu/all_dissertations/3073.
- [44] Michael Persichilli et al. “Supercritical CO₂ Power Cycle Developments and Commercialization: Why sCO₂ can Displace Steam.” In: *Power-Gen India & Central Asia*. 2012.
- [45] X. Petit et al. “Large-eddy simulation of supercritical fluid injection.” In: *The Journal of Supercritical Fluids* 84 (2013), pp. 61–73. ISSN: 0896-8446. DOI: <https://doi.org/10.1016/j.supflu.2013.09.011>. URL: <http://www.sciencedirect.com/science/article/pii/S0896844613003239>.
- [46] Stephen B. Pope. *Turbulent Flows*. Cambridge: Cambridge University Press, 2000.
- [47] Karsten Pruess. *Enhanced Geothermal Systems (EGS) comparing water with CO₂ as heat transmission fluids*. Tech. rep. Lawrence Berkeley National Laboratory, 2007.
- [48] Karsten Pruess and Mohamed Azaroual. “ON THE FEASIBILITY OF USING SUPERCRITICAL CO₂ AS HEAT TRANSMISSION FLUID IN AN ENGINEERED HOT DRY ROCK GEOTHERMAL SYSTEM.” In: *Thirty-First Workshop on Geothermal Reservoir Engineering*. 2006.
- [49] Senthil Kumar Raman et al. “Flow Characteristics of Confined G-CO₂ and S-CO₂ Jets.” In: *Recent Asian Research on Thermal and Fluid Sciences: Proceedings of AJWTF7 2018*. Ed. by Abhilash Suryan et al. Springer Nature Singapore Pte Ltd., 2020, pp. 281–295. ISBN: 123. DOI: https://doi.org/10.1007/978-981-15-1892-8_23. URL: www.
- [50] Florian Ries et al. “Numerical analysis of turbulent flow dynamics and heat transport in a round jet at supercritical conditions.” In: *International Journal of Heat and Fluid Flow* 66 (Aug. 2017), pp. 172–184. DOI: [10.1016/j.ijheatfluidflow.2017.06.007](https://doi.org/10.1016/j.ijheatfluidflow.2017.06.007).
- [51] 8 Rivers. *THE ALLAM-FETVEDT CYCLE*. 2023. URL: <https://8rivers.com/portfolio/the-allam-fetvedt-cycle-and-net-power/>.

- [52] Anthony Ruiz et al. “Numerical Benchmark for High-Reynolds-Number Supercritical Flows with Large Density Gradients.” In: *AIAA Journal* 54 (Nov. 2015), pp. 1445–1460. ISSN: 0001-1452.
- [53] P. Sagaut and R. Grohens. “Discrete filters for large eddy simulation.” In: *International Journal for Numerical Methods in Fluids* 31.8 (1999), pp. 1195–1220. DOI: [10.1002/\(SICI\)1097-0363\(19991230\)31:8<1195::AID-FLD914>3.0.CO;2-H](https://doi.org/10.1002/(SICI)1097-0363(19991230)31:8<1195::AID-FLD914>3.0.CO;2-H).
- [54] Thomas Schmitt et al. “Large-Eddy Simulation of Supercritical-Pressure Round Jets.” In: *AIAA Journal* 48.9 (2010), pp. 2133–2144. DOI: [10.2514/1.J050288](https://doi.org/10.2514/1.J050288). eprint: <https://doi.org/10.2514/1.J050288>. URL: <https://doi.org/10.2514/1.J050288>.
- [55] Uttiya Sengupta. “Fully compressible Direct Numerical Simulations of carbon dioxide close to the vapour- liquid critical point.” PhD thesis. Delft University of Technology, 2019. DOI: [10.4233/uuid:513e5fa7-aef5-47e8-a7f9-d99a06c8981d](https://pure.tudelft.nl/ws/portalfiles/portal/51831002/Thesis.pdf). URL: <https://pure.tudelft.nl/ws/portalfiles/portal/51831002/Thesis.pdf>.
- [56] Huaizhong Shi et al. “Design of experimental setup for supercritical CO₂ jet under high ambient pressure conditions.” In: *Review of Scientific Instruments* 87.12 (2016), p. 125115. DOI: [10.1063/1.4972885](https://doi.org/10.1063/1.4972885). eprint: <https://doi.org/10.1063/1.4972885>. URL: <https://doi.org/10.1063/1.4972885>.
- [57] Hariswaran Sitaraman et al. “Adaptive mesh based combustion simulations of direct fuel injection effects in a supersonic cavity flame-holder.” In: *Combustion and Flame* 232 (2021), p. 111531. ISSN: 0010-2180. DOI: <https://doi.org/10.1016/j.combustflame.2021.111531>. URL: <https://www.sciencedirect.com/science/article/pii/S0010218021002741>.
- [58] Giorgio Soave. “Equilibrium constants from a modified Redlich-Kwong equation of state.” In: *Chemical Engineering Science* 27.6 (1972), pp. 1197–1203. ISSN: 0009-2509. DOI: [https://doi.org/10.1016/0009-2509\(72\)80096-4](https://doi.org/10.1016/0009-2509(72)80096-4). URL: <http://www.sciencedirect.com/science/article/pii/0009250972800964>.
- [59] U.S. Energy Information Administration - EIA - independent statistics and analysis. *Electricity Explained: How electricity is generated*. Nov. 2022. URL: <https://www.eia.gov/energyexplained/electricity/how-electricity-is-generated.php> (visited on 02/19/2023).
- [60] “Supercritical fluid.” In: *Chemical Business* 28.6 (2014), pp. 39–44. ISSN: 09703136. URL: <https://login.proxy.lib.fsu.edu/login?url=http://search.ebscohost.com/login.aspx?direct=true&db=f5h&AN=97302089&site=eds-live&scope=site>.
- [61] Cailin Wang et al. “Experimental study on dispersion behavior during the leakage of high pressure CO₂ pipelines.” In: *Experimental Thermal and Fluid Science* 105 (2019), pp. 77–84. ISSN: 0894-1777. DOI: <https://doi.org/10.1016/j.expthermflusci.2019.03.014>. URL: <http://www.sciencedirect.com/science/article/pii/S0894177719300974>.

- [62] Hai-zhu WANG et al. “Flow field simulation of supercritical carbon dioxide jet: Comparison and sensitivity analysis.” In: *Journal of Hydrodynamics, Ser. B* 27.2 (2015), pp. 210–215. ISSN: 1001-6058. DOI: [https://doi.org/10.1016/S1001-6058\(15\)60474-7](https://doi.org/10.1016/S1001-6058(15)60474-7). URL: <http://www.sciencedirect.com/science/article/pii/S1001605815604747>.
- [63] Song Wang et al. “New Conceptual Design of an Integrated Allam-Cycle Power Complex Coupling Air Separation Unit and Ammonia Plant.” In: *Industrial & Engineering Chemistry Research* 60.49 (2021), pp. 18007–18017. DOI: [10.1021/acs.iecr.1c02478](https://doi.org/10.1021/acs.iecr.1c02478). eprint: <https://doi.org/10.1021/acs.iecr.1c02478>. URL: <https://doi.org/10.1021/acs.iecr.1c02478>.
- [64] Wu Wei, Maozhao Xie, and Ming Jia. “Large eddy simulation of fluid injection under trans-critical and supercritical conditions.” In: *Numerical Heat Transfer, Part A: Applications* 70.8 (2016), pp. 870–886. DOI: [10.1080/10407782.2016.1214485](https://doi.org/10.1080/10407782.2016.1214485). eprint: <https://doi.org/10.1080/10407782.2016.1214485>. URL: <https://doi.org/10.1080/10407782.2016.1214485>.
- [65] N.T. Weiland et al. “12 - Fossil energy.” In: *Fundamentals and Applications of Supercritical Carbon Dioxide (sCO₂) Based Power Cycles*. Ed. by Klaus Brun, Peter Friedman, and Richard Dennis. Woodhead Publishing, 2017, pp. 293–338. ISBN: 978-0-08-100804-1. DOI: <https://doi.org/10.1016/B978-0-08-100804-1.00012-8>. URL: <https://www.sciencedirect.com/science/article/pii/B9780081008041000128>.
- [66] Martin T. White et al. “Review of supercritical CO₂ technologies and systems for power generation.” In: *Applied Thermal Engineering* 185 (2021), p. 116447. ISSN: 1359-4311. DOI: <https://doi.org/10.1016/j.applthermaleng.2020.116447>. URL: <https://www.sciencedirect.com/science/article/pii/S1359431120339235>.
- [67] Yulong Yang et al. “Study on the Impact Pressure of Swirling-Round Supercritical CO₂ Jet Flow and Its Influencing Factors.” In: *Energies* 14.1 (2021). ISSN: 1996-1073. DOI: [10.3390/en14010106](https://doi.org/10.3390/en14010106). URL: <https://www.mdpi.com/1996-1073/14/1/106>.
- [68] Jung Yul Yoo. “The Turbulent Flows of Supercritical Fluids with Heat Transfer.” In: *Annual Review of Fluid Mechanics* 45.1 (2013), pp. 495–525. DOI: [10.1146/annurev-fluid-120710-101234](https://doi.org/10.1146/annurev-fluid-120710-101234). eprint: <https://doi.org/10.1146/annurev-fluid-120710-101234>. URL: <https://doi.org/10.1146/annurev-fluid-120710-101234>.
- [69] Hongyuan Zhang, Ping Yi, and Suo Yang. “Multicomponent Effects on the Supercritical CO₂ Systems: Mixture Critical Point and Phase Separation.” In: *Flow, Turbulence and Combustion* 109 (2022), pp. 515–543. DOI: <https://doi.org/10.1007/s10494-022-00335-9>. URL: <https://link.springer.com/article/10.1007/s10494-022-00335-9#citeas>.
- [70] Huidong Zhang et al. “Investigation on the fluctuation characteristics and its influence on impact force of supercritical carbon dioxide jet.” In: *Energy* 253 (2022), p. 124125. ISSN: 0360-5442. DOI: <https://doi.org/10.1016/j.energy.2022.124125>. URL: <https://www.sciencedirect.com/science/article/pii/S0360544222010283>.

- [71] NAN ZONG and VIGOR YANG*. “CRYOGENIC FLUID JETS AND MIXING LAYERS IN TRANSCRITICAL AND SUPERCRITICAL ENVIRONMENTS.” In: *Combustion Science and Technology* 178.1-3 (2006), pp. 193–227. DOI: [10 . 1080 / 00102200500287613](https://doi.org/10.1080/00102200500287613). eprint: [https : // doi . org / 10 . 1080 / 00102200500287613](https://doi.org/10.1080/00102200500287613). URL: [https : // doi . org / 10 . 1080 / 00102200500287613](https://doi.org/10.1080/00102200500287613).
- [72] Nan Zong et al. “A numerical study of cryogenic fluid injection and mixing under supercritical conditions.” In: *Physics of Fluids* 16.12 (2004), pp. 4248–4261. DOI: [10 . 1063 / 1 . 1795011](https://doi.org/10.1063/1.1795011). eprint: [https : // doi . org / 10 . 1063 / 1 . 1795011](https://doi.org/10.1063/1.1795011). URL: [https : // doi . org / 10 . 1063 / 1 . 1795011](https://doi.org/10.1063/1.1795011).

BIOGRAPHICAL SKETCH

This is my biography.